

# Mesoscale eddies observed by moored current-meters at abyssal depths in the western North Pacific during 1978–1985

Shiro IMAWAKI<sup>1)</sup>\* and Kenzo TAKANO<sup>2)</sup>

**Abstract:** Observations by moored current-meters were carried out repeatedly in mid-ocean of the western North Pacific, providing 50 velocity records. A continuous velocity record for almost seven years was obtained at 5000 m depth. The overall mean velocity is directed to the north with a speed of less than  $1 \text{ cm s}^{-1}$ . The kinetic energy of low-frequency velocity-fluctuations, or mesoscale eddies is more than 30 times larger than that of mean flow. Frequency spectra of eddy kinetic energy show that most of the energy is contained in mesoscale bands (periods of 31–235 days), with zonal (meridional) dominance of energy in the longer (shorter) period band. An array observation at 4000 m depth shows that the local change of relative vorticity of mesoscale eddies is balanced mainly with the advection of planetary vorticity, although the horizontal advection of relative vorticity and higher-order horizontal divergence may play some role. Those results suggest that the mesoscale eddies are understood as primarily plane barotropic Rossby waves with possible modification.

**Keywords :** *mesoscale eddies, moored current-meter, frequency spectrum, vorticity balance*

## 1. Introduction

Synoptic current fluctuations having typical temporal scales of weeks to months and horizontal scales of tens to hundreds of kilometers are called “mesoscale eddies.” They are also called “low-frequency fluctuations” or “low-frequency eddies.” Mesoscale eddies dominate in the mid-ocean flow field (ROBINSON, 1983). They were first recognized from observations in 1959 by neutrally-buoyant floats at mid-depths in the North Atlantic (CREASE, 1962). They have been measured by moored current-meters and neu-

trally-buoyant floats at depth, most intensively in 1970s and 1980s. The highlight was the Mid-Ocean Dynamics Experiment (MODE) carried out in 1973 in the western North Atlantic (MODE GROUP, 1978). Mesoscale eddies at surface layers have been measured by surface drifting-buoys tracked by satellites (NILER, 2001). Since the Topex/Poseidon satellite was launched in 1992, mesoscale eddies have been intensively measured by satellite altimeters; details of mesoscale eddies with surface manifestation have been revealed, especially for their global views (FU and MORROW, 2013).

To understand the nature of mesoscale eddies, their mechanisms and their roles in ocean circulation, observations at depth are necessary as well as surface observations. A considerable

---

1) Professor Emeritus of Kyushu University, Yokohama, 224-0014, Japan

2) Matsudo, Chiba Prefecture, 271-0064, Japan

\*Corresponding author:

E-mail: imawaki@g04.itscom.net

fraction of velocity and temperature fluctuations observed in the MODE area is accounted for by a combination of barotropic and first-mode baroclinic Rossby waves (MCWILLIAMS and FLIERL, 1976). In the Gulf Stream recirculation region in the North Atlantic, a barotropic Rossby wave modified by bottom topography was observed beneath the thermocline (PRICE and ROSSBY, 1982). At a site called R to the east of the Izu-Ogasawara Ridge in the western North Pacific, a considerable fraction of mesoscale eddies at abyssal depths is accounted for by a set of three barotropic Rossby waves (IMAWAKI, 1985). Recent studies show that fluctuations at the same site having specific spectral peaks are explained by plane topographic Rossby waves (MIYAMOTO *et al.*, 2017; 2019). Under the Kuroshio Extension, topographic Rossby waves in a period band of 30–60 days were observed (GREENE *et al.*, 2012).

Examination of vorticity balance of mesoscale eddies at 1500 m depth in the MODE area shows that a 10-day mean balance is highly nonlinear but a 60-day mean balance is marginally linear (MCWILLIAMS, 1976). In the North Equatorial Current region in the Atlantic, the local change of relative vorticity is balanced with the advection of planetary vorticity in the thermocline as well as in the deep layer, for a period band of 24–81 days (KEFFER, 1983). At the Site R to the east of the Izu-Ogasawara Ridge, the local change of relative vorticity is accounted for by the advection of planetary vorticity at 5000 m depth within the estimated error (IMAWAKI, 1983).

These studies suggest that the dynamics of mid-ocean mesoscale eddies differs at locations, depths and temporal/spatial scales, and further examinations are required to understand the eddy field. Intensive observations by moored current-meters were carried out at abyssal depths at more than 20 stations in the Site R during

1978–1985, in order to primarily investigate mesoscale eddies. The present paper provides description of the velocity measurements and results obtained mostly on mesoscale eddies.

The rest of the paper is organized as follows. Section 2 describes the observation site, mooring operations, current measurements and data processing. Section 3 gives general statistics of individual velocity records and describes combining individual records. Section 4 shows features of mean flows. Section 5 describes statistical features of mesoscale eddies. Section 6 shows features of frequency spectra. Section 7 describes the vorticity balance of mesoscale eddies using the current-meter data, with Subsection 7.1 on Array-83 and Subsection 7.2 on Array-84. Sections 8 and 9 are discussions and summary, respectively.

## 2. Current measurements

The observation site called R is centered at 30°N, 147°E in the western North Pacific. At shallow depths, the site center is located about 400 km south of the Kuroshio Extension (Fig. 1) and on the indistinct southern boundary of the broad west-southwestward flowing Kuroshio Countercurrent (UCHIDA and IMAWAKI, 2003). At abyssal depths, it is sufficiently distant from the weak deep western boundary current located east of the Izu-Ogasawara Ridge (KAWABE and FUJIO, 2010). Like the MODE area, the observation site is located between a strong current region and the interior.

Figure 1 also shows bottom topography based on ETOPO1 (AMANTE and EAKINS, 2009). The site center is located about 500 km east of the Izu-Ogasawara Ridge. The water depth varies between 6000 and 6300 m within 100 km of the center. The bottom topography is generally flat with small gentle undulations and no apparent large-scale slopes. Exception is several sea-

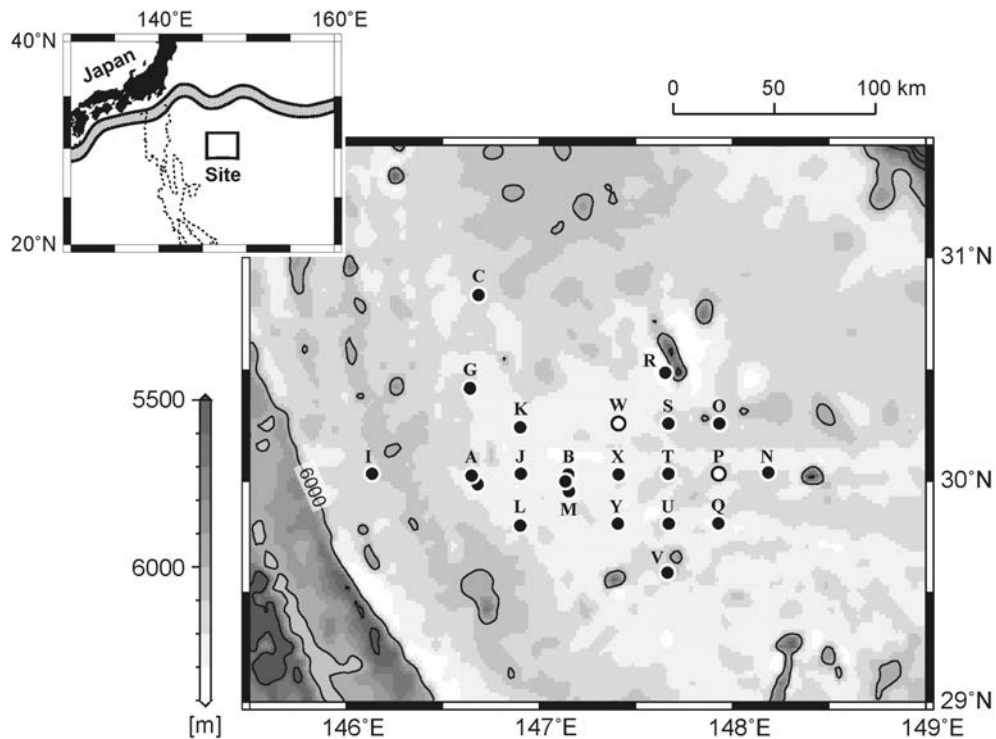


Fig. 1 Location of mooring stations with bottom topography. Dots with station names show locations where current-meter data were obtained; the first “R” of station names is omitted. Two open circles show locations where moorings were deployed but not recovered in Obs. 9. Darker gray indicates shallower depth, with contours of 500 m interval. The rectangle within the small-scale physiographic inset illustrates the location of the present study area relative to both the Kuroshio system, whose mean path during 1993–2000 is shown by shading, and the Izu-Ogasawara Ridge, whose horizontal extent at 3000 m depth is shown by dotted lines.

mounts, for example, a small seamount near Stn. RR, which was not known at the observation time.

Configuration of a used conventional intermediate mooring is shown in Fig. 2 schematically. The mooring line with current-meters inserted was designed to be held vertical in fluctuating flows by both large buoyancy of a glass-sphere cluster at the top and dead weight on the seabed. The mooring was deployed by the so-called “buoy-first/anchor-last” way. It was recovered by releasing an anchor weight through a command from the ship to an acoustic release. When

the mooring line surfaced, a radio-transmitter sent a radio signal to the ship to be located. The mooring technology had been developed by the Buoy Group of Woods Hole Oceanographic Institution (HEINMILLER, 1976) and was transferred to Japan in mid 1970s.

Numbers of current-meters were moored mostly at abyssal depths at various locations in Site R (Fig. 1) repeatedly during 1978 through 1985. Table 1 shows the summary of mooring operations. First moorings were deployed in October 1978. In March 1979, they were recovered and second moorings were deployed on the same

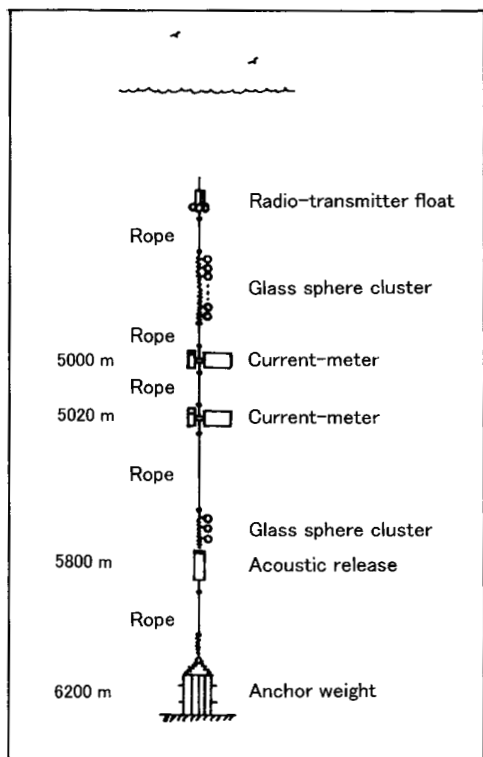


Fig. 2 Schematic view of an intermediate mooring, deployed at 6200 m depth as an example.

cruise. Such recovery and deployment cruises were repeated. Finally, last moorings were recovered in July 1985. As a result, nine mooring observations were performed; they are called Obs. 1 through 9.

Totally 44 moorings were deployed. Thirty-two of them were recovered successfully to provide numbers of good quality records. Two others were recovered without useful records. Ten were not recovered, mostly in Obs. 3, probably because anchor weights made of bundling cut-rails were taken apart during mooring. Therefore, the recovery rate of mooring is 77 % as a whole; it increases to 87 % if Obs. 3 is excluded. Data were not retrieved successfully from 13 current-meters on 12 recovered moorings; they are not listed in Table 1. Totally 50 records are

available. Measurements were restricted mostly to abyssal depths because our mooring technology at that time did not allow us to obtain safe and stable platforms at shallow depths.

Aanderaa RCM-5 current-meters were moored. The current-meter measured current speed by a Savonius rotor and current direction by a magnetic compass, which detected the direction of the instrument body following the fluctuating flow freely. The current-meter recorded current speed, current direction and temperature on a small magnetic tape at an interval of mostly one hour.

After the recovery, the data were linearly interpolated in time, in order to correct possible gain or delay of the inside clock and provide the data every hour on the hour, if recording had continued until the recovery; the discrepancy was typically less than one hour. The reference of flow direction was transferred from the magnetic north to the true north; the magnetic north was located to 2-3° W at the present site. Then noises and doubtful data were removed by eye.

An example of raw data from a nominal depth of 4000 m is shown in Fig. 3 (a). [The current-meter depth is hereafter understood as "nominal."] The velocity record shows very regular oscillations, for example, during year-days -50 to -30; the flow direction changes clockwise quite regularly. The average oscillation period during that part is estimated to be 24.3 h, which is close to the local inertial period (theoretical period of inertial oscillation) at 30° N (23.93 h). Those local inertial oscillations are ubiquitous in velocity records obtained. Temperature data are not used in the present study.

In the raw data, diurnal and semi-diurnal tidal fluctuations are apparent as well as inertial oscillations. Those high-frequency fluctuations in the eastward ( $u$ ) and northward ( $v$ ) velocity-components are filtered out by Godin filter (GODIN,

**Table 1.** Summary of mooring observations at Site R during 1978–1985. Listed are 32 successfully recovered moorings with at least one current-meter providing a good quality record. The time coordinate is Japan Standard Time.

Obs. No.	Stn.	Location		Water depth (m)	Nominal depth (m) of current-meter	Deployment Date and Cruise*	Recovery Date and Cruise*	Duration (days)
		Lat. (N)	Long. (E)					
1	RA	29° 59.2'	146° 40.7'	6210	4000, 5000	1 Oct. 1978 H	17 Mar. 1979 H	167
	RB	30° 00.1'	147° 08.6'	6240	4000, 5000	2 Oct. 1978 H	19 Mar. 1979 H	168
	RC	30° 49.8'	146° 41.1'	6180	4000, 5000	2 Oct. 1978 H	17 Mar. 1979 H	166
2	RB	29° 59.9'	147° 07.6'	6220	4000, 4500, 5000, 5180	19 Mar. 1979 H	21 Nov. 1979 T	247
	RC	30° 49.3'	146° 41.6'	6170	4000	17 Mar. 1979 H	21 Nov. 1979 T	249
3	RB	29° 56.4'	147° 08.2'	6210	4000	21 Nov. 1979 T	23 Aug. 1980 T	276
4	RA	30° 01.8'	146° 38.2'	6210	650, 1500, 3000, 5000	28 Sept. 1980 H	19 July 1981 T	294
	RB	29° 54.8'	147° 08.3'	6220	5000	24 Aug. 1980 T	19 July 1981 T	329
	RG	30° 25.0'	146° 38.4'	6180	5000	25 Aug. 1980 T	19 July 1981 T	327
	RI	30° 02.2'	146° 07.3'	6110	5000	25 Aug. 1980 T	18 July 1981 T	327
5	RB	30° 02.0'	147° 09.0'	6260	4980, 5000	19 July 1981 T	18 July 1982 B	364
	RI	30° 01.7'	146° 07.5'	6090	5000	20 July 1981 T	17 July 1982 B	362
6	RB	30° 02.1'	147° 09.0'	6250	5000	18 July 1982 B	15 May 1983 H	301
	RI	30° 02.8'	146° 07.9'	6070	5000	19 July 1982 B	13 May 1983 H	298
7	RA	30° 01.1'	146° 39.4'	6230	4000, 4020	14 May 1983 H	25 Oct. 1983 B	164
	RB	30° 00.5'	147° 09.1'	6250	4000, 5000	15 May 1983 H	25 Oct. 1983 B	163
	RJ	30° 02.0'	146° 54.1'	6260	4000, 4020	14 May 1983 H	25 Oct. 1983 B	164
	RK	30° 14.6'	146° 54.0'	6210	4000	15 May 1983 H	24 Oct. 1983 B	162
	RL	29° 48.0'	146° 54.0'	6150	4000, 4020	14 May 1983 H	27 Oct. 1983 B	166
8	RB	30° 02.4'	147° 09.1'	6250	5000	25 Oct. 1983 B	2 July 1984 B	251
	RM	29° 57.3'	147° 09.1'	6210	5000	27 Oct. 1983 B	2 July 1984 B	249
9	RB	30° 01.9'	147° 08.9'	6260	5000	3 July 1984 B	1 July 1985 B	363
	RN	30° 02.4'	148° 11.0'	6200	4000	5 July 1984 B	4 July 1985 B	364
	RO	30° 15.6'	147° 55.8'	6180	4000	7 July 1984 B	2 July 1985 B	360
	RQ	29° 48.6'	147° 55.5'	6230	4000	5 July 1984 B	4 July 1985 B	364
	RR	30° 29.1'	147° 39.0'	6320	4100, 4120	7 July 1984 B	2 July 1985 B	360
	RS	30° 15.6'	147° 40.0'	6180	4000, 4020	7 July 1984 B	2 July 1985 B	360
	RT	30° 02.0'	147° 40.0'	6160	4000	6 July 1984 B	3 July 1985 B	362
	RU	29° 48.5'	147° 40.1'	6160	4000, 4020	4 July 1984 B	3 July 1985 B	364
	RV	29° 35.2'	147° 39.7'	6200	4020	4 July 1984 B	3 July 1985 B	364
	RX	30° 01.9'	147° 24.5'	6250	4000	3 July 1984 B	1 July 1985 B	363
RY	29° 48.5'	147° 24.3'	6210	4000, 4020	4 July 1984 B	1 July 1985 B	362	

\* H: *Hakuho Maru*, T: *Tokaidai-gaku Maru II*, B: *Bosei Maru II*.

1972) for analyses on the low-frequency fluctuations. Figure 4 shows the shape of Godin filter and its power gain. The shape comes from taking running-means of hourly data three times over 24, 24 and 25 data repeatedly; the filter consists of 71 terms. Therefore, the filter guarantees almost complete removal of diurnal and semi-diurnal tidal fluctuations, although the response

with half power gain at 3.9 days is not satisfactorily sharp. The inertial period at the present site varies between 23.34 h (Stn. RC) and 24.24 h (Stn. RV), and therefore, Godin filter can remove inertial oscillations effectively as well. Figure 3 (b) shows low-pass-filtered data of the raw data shown in Fig. 3 (a).

After the high-frequency fluctuations are fil-

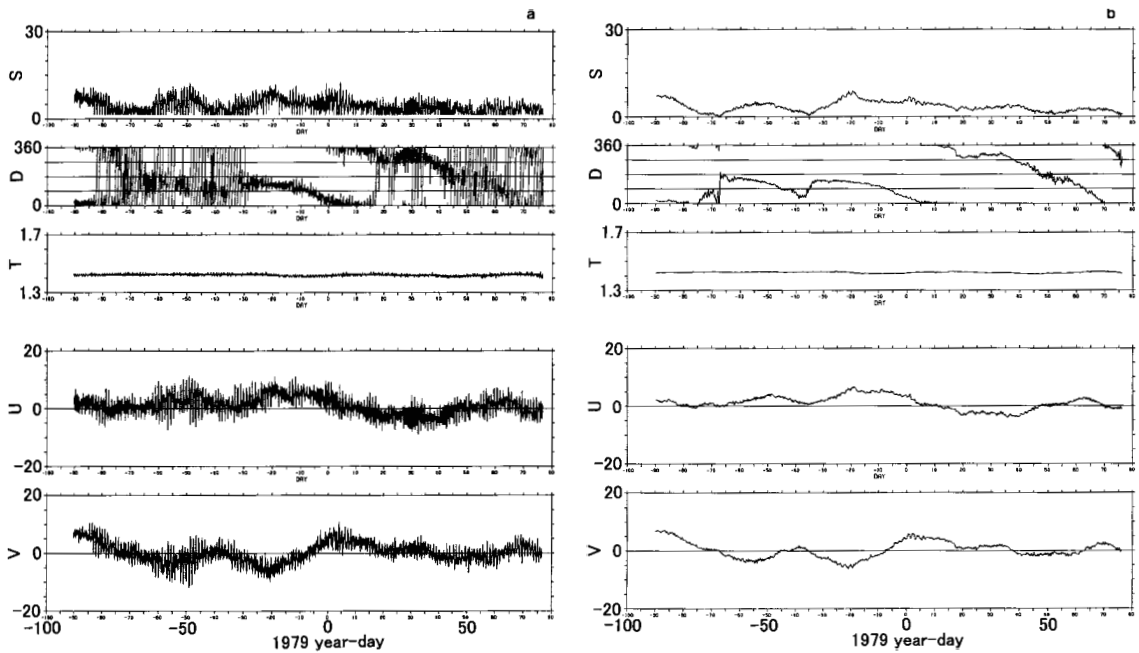


Fig. 3 Time series of velocity and temperature observed at 4000 m depth at Stn. RA during Obs. 1. Panel (a) is the raw data sampled at 30-minute interval and (b) their low-pass-filtered data. From top to bottom in each panel, current speed ( $S$ ;  $\text{cm s}^{-1}$ ), current direction ( $D$ ; degrees, clockwise from the true north), temperature ( $T$ ; degrees Celsius), eastward velocity-component ( $U$ ;  $\text{cm s}^{-1}$ ) and northward one ( $V$ ;  $\text{cm s}^{-1}$ ) are shown. The abscissa is time in year-day of 1979, or the serial day from 1 January 1979.

tered out, data are subsampled at midnight of Japan Standard Time to provide the daily data. The aliasing due to fluctuations with periods between one and two days is small because the response of the filter is not sharp. The measurement error of these low-pass-filtered data is estimated to be  $0.43 \text{ cm s}^{-1}$  for both  $u$  and  $v$  components, from standard deviations of differences between two sets of velocity data obtained at almost same depths (only 20 m apart vertically) near 4000 or 5000 m depth on the same mooring lines at eight stations (Table 2). For those pairs of data sets, the raw data are also almost identical with each other.

### 3. General statistics and combining records

Table 2 shows the general statistics of all the

50 records obtained at 19 stations (Fig. 1). All calculations are done for the low-pass-filtered daily velocities. Statistics for Obs. 1 have already been reported (IMAWAKI, 1985). At abyssal depths (at 4000 m or deeper), the mean flow is weak and therefore, the kinetic energy per unit mass for the mean flow, or mean kinetic energy ( $K_M$ ) is small; it varies between  $0.1$  and  $5.6 \text{ cm}^2 \text{ s}^{-2}$ . The kinetic energy per unit mass for meso-scale eddies, or eddy kinetic energy ( $K_E$ ) varies between  $5$  and  $24 \text{ cm}^2 \text{ s}^{-2}$ ; it is an order of magnitude larger than the  $K_M$ . This indicates that the site is located in the mid-ocean.

Time-space averages of those individual statistics at abyssal depths are calculated with weight of measurement duration and listed at the bottom of Table 2. The present 47 records at abys-

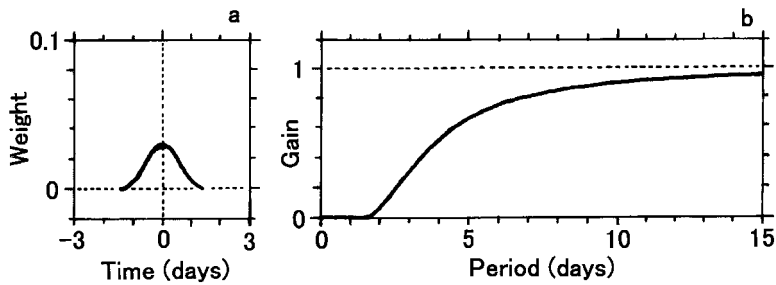


Fig. 4 Godin filter. Panel (a) shows the distribution of weights to be put on 71 hourly data. Panel (b) shows the square of filter response factor as a function of fluctuation period.

sal depths provide the sum of 11,660 day (32 year) data. Records obtained at several depths at the same station may not be independent from each other for the low-frequency fluctuations and therefore, incomplete records are excluded first, if any, and then remaining complete records are weighted to represent one record at that station, except for Stn. RY, where the longer record is chosen. The data used for calculation of averages are totally 8830 day (24 year) data, and therefore, those statistics are considered to be representative values at the present site. The time-space average  $u$  and  $v$  components ( $-0.29$  and  $0.71 \text{ cm s}^{-1}$ , respectively) are small. The average zonal and meridional variances ( $10$  and  $11 \text{ cm}^2 \text{ s}^{-2}$ , respectively) are almost equal to each other. The  $K_E$  ( $11 \text{ cm}^2 \text{ s}^{-2}$ ) is about 40 times larger than the  $K_M$  ( $0.3 \text{ cm}^2 \text{ s}^{-2}$ ). Note that the  $K_M$  listed in the table is calculated from the average  $u$  and  $v$  components; the average of individual  $K_M$ 's is  $1.5 \text{ cm}^2 \text{ s}^{-2}$ .

For shallower flow field, three records were obtained at 650, 1500 and 3000 m depths at Stn. RA during Obs. 4. The record at 3000 m depth shows very similar features to those at 5000 m depth, in the time series of low-pass-filtered velocity and the general statistics. The record at 1500 m depth is too short to discuss mesoscale eddies but the hourly raw data shows an inter-

esting phenomenon of unusually long-lived inertial oscillation. The flow direction continues to change clockwise quite regularly for more than 40 days without any major disturbances or interruption (not shown here). The average oscillation period is estimated to be 22.8 h (41.8 days for 44 cycles), which is a little shorter than the local inertial period of 23.93 h. The record at 650 m depth shows quite different features; zonal and meridional variances and  $K_E$  are several times larger than those at 5000 m depth (Table 2).

At Stn. RB, moored current-meters were maintained continuously during all the nine observations; each mooring was located within 10 km from the mean position. By combining those records, a long continuous record was obtained at 5000 m depth for 2462 days (6.7 years) from October 1978 through June 1985 as shown in Fig. 5. For Obs. 3, no current-meter was moored at 5000 m depth, and it is justifiably made up for by the record at 4000 m depth, because low-pass-filtered daily velocities at those abyssal depths at the same station are similar to each other as shown at beginnings of Sections 4 and 5. At Stn. RC, a continuous record was obtained at 4000 m depth for 411 days from October 1978 through November 1979; each mooring was located within 1 km from the mean position. At Stn. RI, a con-

**Table 2.** Statistics of low-pass-filtered daily velocities from 50 individual records. Symbol  $u$  ( $v$ ) denotes eastward (northward) velocity-component; overbar denotes temporal average over the record length and prime denotes deviation from it;  $K_M$  ( $K_E$ ) denotes mean (eddy) kinetic energy. Time-space averages of those individual statistics at abyssal depths (see the text) are shown at the bottom.

Obs. No.	Stn.	Depth (m)	First data	Last data	Duration (days)	$\bar{u}$	$\bar{v}$	$K_M$	$\overline{u'^2}$	$\overline{v'^2}$	$K_E$	$\overline{u'v'}$
						(cm s <sup>-1</sup> )	(cm <sup>2</sup> s <sup>-2</sup> )		(cm <sup>2</sup> s <sup>-2</sup> )	(cm <sup>2</sup> s <sup>-2</sup> )		(cm <sup>2</sup> s <sup>-2</sup> )
1	RA	4000	4 Oct. 1978	16 Mar. 1979	164	1.1	0.3	0.6	5.6	7.7	6.6	-2.3
		5000	4 Oct. 1978	3 Mar. 1979	151*	1.2	-0.3	0.8	5.6	8.0	6.8	-2.3
	RB	4000	4 Oct. 1978	18 Mar. 1979	166	0.2	-0.4	0.1	9.0	9.5	9.3	0.4
		5000	4 Oct. 1978	18 Mar. 1979	166	-0.0	-0.4	0.1	7.9	9.2	8.6	-0.2
	RC	4000	5 Oct. 1978	15 Mar. 1979	162	-1.3	2.1	3.0	9.3	14.3	11.8	1.6
		5000	5 Oct. 1978	15 Mar. 1979	162	-1.8	2.0	3.7	9.4	11.8	10.6	1.4
2	RB	4000	22 Mar. 1979	8 Oct. 1979	201*	-0.8	-0.4	0.4	6.9	6.0	6.5	-1.7
		4500	22 Mar. 1979	20 Oct. 1979	213*	-0.3	-0.2	0.1	8.5	6.3	7.4	-0.9
		5000	22 Mar. 1979	20 Nov. 1979	244	-0.3	0.2	0.1	8.5	7.6	8.1	-1.8
		5180	22 Mar. 1979	20 Nov. 1979	244	-0.2	0.3	0.1	8.2	7.6	7.9	-1.9
	RC	4000	19 Mar. 1979	19 Nov. 1979	246	-1.0	-0.2	0.5	13.1	20.1	16.6	-2.6
3	RB	4000	24 Nov. 1979	22 Aug. 1980	273	-0.6	0.6	0.4	5.3	6.8	6.1	-1.0
4	RA	650	1 Oct. 1980	17 July 1981	290	0.0	1.2	0.7	38.6	33.1	35.9	6.8
		1500	8 Nov. 1980	22 Dec. 1980	45*	0.1	0.1	0.0	7.9	1.8	4.8	0.9
		3000	1 Oct. 1980	17 July 1981	290	-0.3	0.4	0.1	4.4	6.5	5.4	-2.0
		5000	1 Oct. 1980	17 July 1981	290	-0.3	-0.6	0.2	4.8	7.8	6.3	-2.5
	RB	5000	26 Aug. 1980	17 July 1981	326	-1.0	0.4	0.5	4.3	6.1	5.2	-1.9
	RG	5000	28 Aug. 1980	16 July 1981	323	-0.7	-0.1	0.2	8.5	15.1	11.8	-2.1
	RI	5000	27 Aug. 1980	17 July 1981	325	-0.9	2.3	3.0	4.3	16.8	10.5	-0.2
5	RB	4980	22 July 1981	23 Oct. 1981	94*	0.7	0.2	0.3	6.2	8.3	7.2	2.5
		5000	22 July 1981	16 July 1982	360	-0.1	1.0	0.5	9.3	9.2	9.3	-2.8
	RI	5000	23 July 1981	15 July 1982	358	-0.3	2.5	3.2	8.2	18.0	13.1	1.7
6	RB	5000	21 July 1982	13 May 1983	297	0.9	1.0	1.0	15.2	9.2	12.2	1.2
	RI	5000	22 July 1982	12 May 1983	295	-0.7	2.9	4.3	4.0	5.5	4.8	-2.2
7	RA	4000	17 May 1983	23 Oct. 1983	160	-0.8	-1.1	0.9	11.6	5.4	8.5	2.1
		4020	17 May 1983	23 Oct. 1983	160	-0.9	-1.4	1.3	14.1	7.3	10.7	1.4
		4000	17 May 1983	24 Oct. 1983	161	-0.8	1.3	1.2	11.7	7.8	9.7	3.9
	RB	4000	17 May 1983	24 Oct. 1983	161	-0.5	0.9	0.5	12.3	8.3	10.3	4.5
		5000	17 May 1983	24 Oct. 1983	161	-0.7	0.1	0.3	9.9	6.3	8.1	3.2
	RJ	4000	17 May 1983	23 Oct. 1983	160	-0.7	0.1	0.3	9.9	6.3	8.1	3.2
		4020	17 May 1983	23 Oct. 1983	160	-0.6	0.0	0.2	11.2	5.1	8.2	1.7
	RK	4000	18 May 1983	23 Oct. 1983	159	-1.1	0.2	0.6	13.3	7.0	10.2	0.2
	RL	4000	17 May 1983	25 Oct. 1983	162	-0.3	-0.6	0.2	10.6	6.5	8.6	2.8
4020		17 May 1983	25 Oct. 1983	162	-0.4	-0.4	0.1	8.9	5.5	7.2	2.9	
8	RB	5000	28 Oct. 1983	1 July 1984	248	-0.1	1.2	0.7	9.7	6.2	8.0	-3.3
	RM	5000	30 Oct. 1983	1 July 1984	246	0.2	0.9	0.5	7.2	5.0	6.1	-1.5
9	RB	5000	6 July 1984	30 June 1985	360	0.4	1.0	0.6	12.7	12.0	12.4	-2.9
	RN	4000	8 July 1984	2 July 1985	360	-1.0	-0.3	0.5	12.4	10.0	11.2	-0.8
	RO	4000	9 July 1984	1 July 1985	358	1.8	0.1	1.6	15.9	17.3	16.6	-3.2
	RQ	4000	8 July 1984	2 July 1985	360	-2.3	0.2	2.6	9.1	9.4	9.3	-1.5
	RR	4100	10 July 1984	1 July 1985	357	2.9	-0.1	4.1	6.7	23.4	15.1	-4.8
		4120	10 July 1984	1 July 1985	357	2.8	0.2	3.9	7.4	21.5	14.4	-6.1
	RS	4000	10 July 1984	30 June 1985	356	2.5	0.8	3.4	19.1	21.5	20.3	-4.3
		4020	10 July 1984	2 Apr. 1985	267*	3.3	0.7	5.6	22.2	25.5	23.9	-6.5
	RT	4000	9 July 1984	1 July 1985	358	-0.7	1.2	0.9	14.3	13.4	13.9	-2.2

RU	4000	7 July 1984	1 July 1985	360	-2.0	0.6	2.2	10.4	10.6	10.5	-0.6
	4020	7 July 1984	19 Oct. 1984	105*	-2.8	1.5	5.1	14.3	3.3	8.8	0.9
RV	4020	7 July 1984	18 Nov. 1984	135*	-3.0	0.7	4.7	11.4	2.2	6.8	-0.4
RX	4000	6 July 1984	7 June 1985	337*	-0.3	1.4	1.0	14.9	13.0	14.0	-0.5
RY	4000	6 July 1984	7 June 1985	337*	-1.4	0.9	1.4	12.0	9.1	10.5	-1.2
	4020	6 July 1984	16 Mar. 1985	254*	-1.3	0.8	1.1	11.9	11.2	11.6	-0.9
Time-space average					-0.29	0.71	0.29	10.19	11.37	10.79	-1.32

\* Incomplete record which stopped before recovery due to battery trouble or instrumental failure

**Table 3.** Summary and statistics of long continuous records obtained by combining successive records. See Table 2 for notations.

Stn.	Mean location		Water depth (m)	Meter depth (m)	First deployment	Last recovery	Obs. No.	Duration (days)
	Lat. (N)	Long. (E)						
RB	30° 00'	147° 08'	6240	5000*	2 Oct. 1978	1 July 1985	1 - 9	2464
RC	30° 50'	146° 41'	6170	4000	2 Oct. 1978	21 Nov. 1979	1, 2	415
RI	30° 02'	146° 08'	6090	5000	25 Aug. 1980	13 May 1983	4 - 6	992

Stn.	Meter depth (m)	First data	Last data	Duration (days)	$\bar{u}$	$\bar{v}$	$K_M$	$\overline{u'^2}$	$\overline{v'^2}$	$K_E$	$\overline{u'v'}$
					(cm s <sup>-1</sup> )	(cm <sup>2</sup> s <sup>-2</sup> )		(cm <sup>2</sup> s <sup>-2</sup> )	(cm <sup>2</sup> s <sup>-2</sup> )		
RB	5000*	4 Oct. 1978	30 June 1985	2462	-0.12	0.72	0.27	9.8	8.5	9.2	-1.2
RC	4000	5 Oct. 1978	19 Nov. 1979	411	-1.06	0.73	0.83	11.6	18.9	15.3	-1.1
RI	5000	27 Aug. 1980	12 May 1983	989	-0.66	2.53	3.42	5.8	14.0	9.9	-0.2

\* For Obs. 3, velocities at 4000 m depth are used instead of 5000 m (see the text).

tinuous record was obtained at 5000 m depth for 989 days (2.7 years) from August 1980 through May 1983; each mooring was located within 2 km from the mean position. Table 3 shows the statistics of the three records. A part of the present time series of daily velocity has already been published (IMAWAKI and TAKANO, 1982; MIYAMOTO *et al.*, 2017).

#### 4. Mean flows

Differences of mean velocities between 4000 and 5000 m depths at the same station are small in five available comparison cases at Stns. RA, RB and RC (Table 2); standard deviations of differences of mean  $u$  and  $v$  components between the two depths are both 0.40 cm s<sup>-1</sup>, which is the same level as the estimated measurement error (Section 2). That is to say mean velocities at

abyssal depths at the same station are similar to each other.

Figure 6 shows horizontal distribution of mean velocities at abyssal depths. A striking feature is the large anticyclonic vortex observed during Obs. 9 at 11 stations east of Stn. RB. This steady vortex, however, is beyond the scope of the present paper and described on a separate paper (IMAWAKI and TAKANO, 2019). The mean  $v$  component at Stn. RI (2.5 cm s<sup>-1</sup>) is remarkably large. It comes from a stable mean flow toward north-northwest; means of  $v$  component during Obs. 4, 5 and 6 are 2.3, 2.5 and 2.9 cm s<sup>-1</sup>, respectively (Table 2).

At Stn. RB, nine observations were carried out continuously (Table 1 and Fig. 5). The mean velocity during each observation is shown in Fig. 7. Those mean velocities are weak and their maxi-

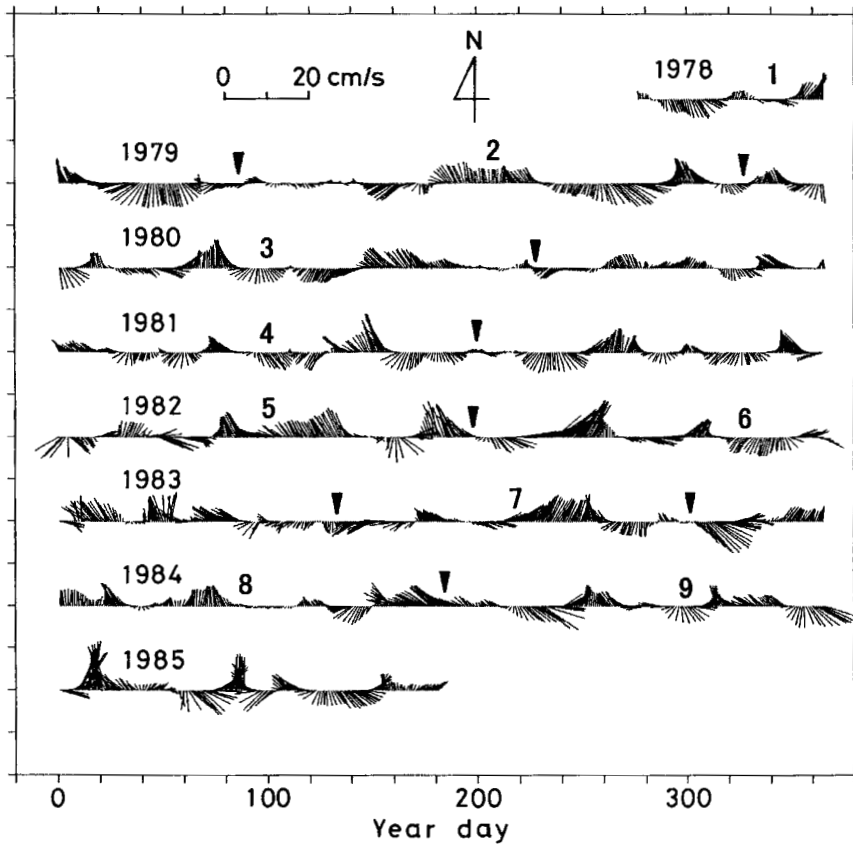
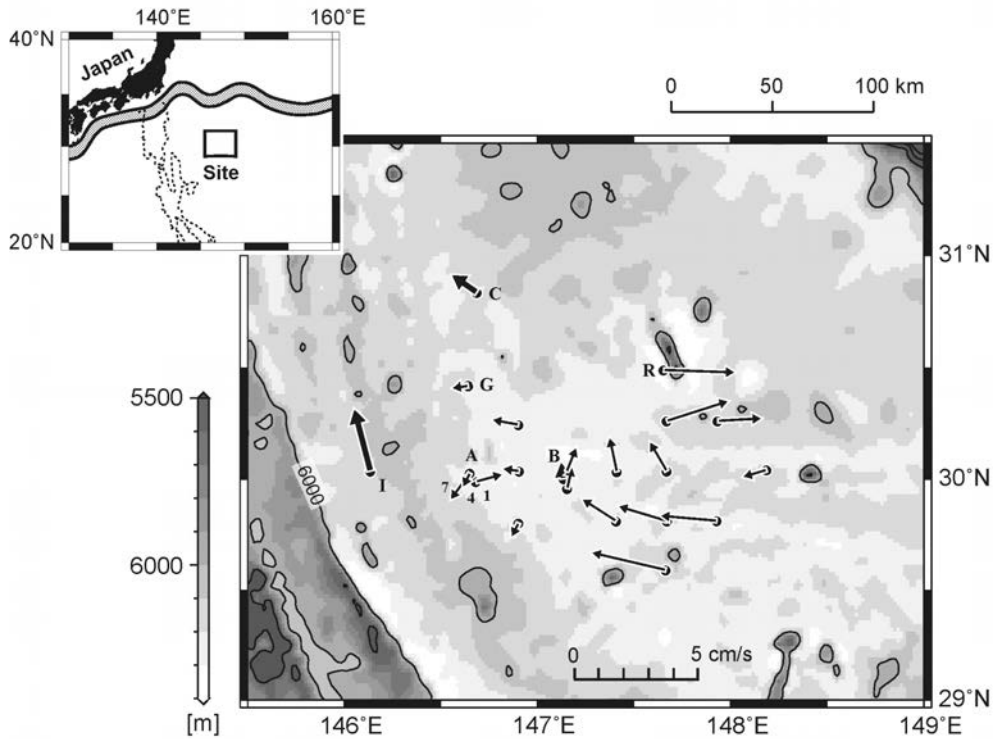


Fig. 5 Time series of low-pass-filtered daily velocity obtained at 5000 m depth at Stn. RB from 4 October 1978 through 30 June 1985. For Obs. 3, velocities at 4000 m depth are used. Each stick represents a daily velocity vector (upward north). The abscissa is time in year-day. Arrowheads indicate exchange of moorings. Numerals indicate observation numbers.

mum speed is only  $1.4 \text{ cm s}^{-1}$  during Obs. 6. Their  $v$  components are positive, except during Obs. 1. Their combined record shows followings (Table 3). The overall mean velocity during seven years is less than  $1 \text{ cm s}^{-1}$  in speed and directed to the north; the mean  $u$  ( $v$ ) component is  $-0.12$  ( $0.72$ )  $\text{cm s}^{-1}$  (Fig. 7). The  $K_M$  ( $0.3 \text{ cm}^2 \text{ s}^{-2}$ ) is very small. Those statistics are quite similar to the time-space averages of all individual statistics at abyssal depths (Table 2).

Errors of those estimated mean  $u$  and  $v$  components due to low-frequency fluctuations are

evaluated at the 95 % confidence level, following ZENK and MÜLLER (1988) and TALLEY *et al.* (2011), as follows. The standard error  $S_e$  is given by  $\sigma_0 / \sqrt{N_d}$ , where  $\sigma_0$  is the standard deviation of the original time series and  $N_d$  the degrees of freedom. The degrees of freedom is given by  $T_r / \tau_i$ , where  $T_r$  is the record length and  $\tau_i$  the integral timescale estimated approximately by integrating the autocorrelation function until its first zero-crossing. Assuming normal distribution, the error  $\varepsilon$  of the estimated mean at the 95 % confidence level is given by  $t_s S_e$ , where  $t_s$ ,



**Fig. 6** Horizontal distribution of mean velocities at abyssal depths during individual observations (thin arrows; Table 2) and those from three combined records (thick arrows; Table 3). Velocities at 4000 m depth are shown, except 5000 m depth velocities at Stns. RB, RG and RI, and for Obs. 4 at Stn. RA. Three arrows at Stn. RA are for Obs. 1, 4 and 7. At Stn. RB, the mean velocity during Obs. 9 is shown as well as that from the combined record. Selected station names are shown with the first “R” omitted. Darker gray indicates shallower depth, with contours of 500 m interval.

the Student’s  $t$ -variable is about 2.0 when the degrees of freedom is larger than 27. Those properties for the present combined record at Stn. RB are shown in Table 4. The mean  $v$  component ( $0.72 \pm 0.35 \text{ cm s}^{-1}$ ) is positive significantly, while the mean  $u$  component ( $-0.12 \pm 0.44 \text{ cm s}^{-1}$ ) is not significantly different from zero. Estimated means also include the measurement error, which is not discussed here.

It is interesting to examine how a shorter-term “mean” fluctuates around a long-term mean, which is regarded to be closer to the true mean, and how it converges with increasing data

used, on real data. The present seven-year long data can provide many “means” estimated for shorter durations. For example, “means” for 200 days can be estimated in 12 independent cases; the “mean”  $u$  ( $v$ ) components vary between  $-1.6$  and  $2.2 \text{ cm s}^{-1}$  ( $-0.4$  and  $1.7 \text{ cm s}^{-1}$ ) with standard deviation of  $1.0$  ( $0.6$ )  $\text{cm s}^{-1}$ . Dependence of standard deviation of those “means” upon the length of data used for estimation is shown in Fig. 8. The figure also shows the standard error  $S_e$  as a function of record length. The standard deviation decreases with increasing data length quite similarly to the standard error, al-

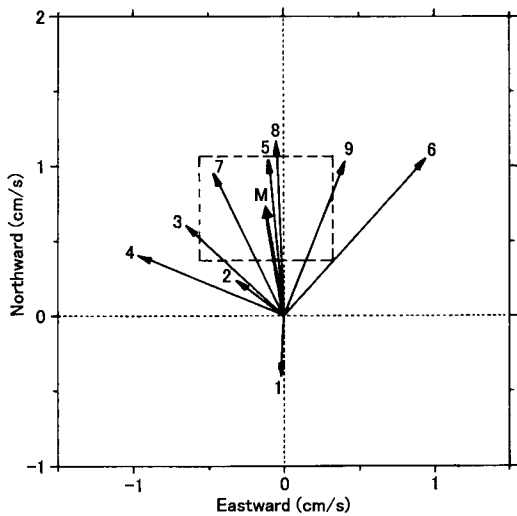


Fig. 7 Mean velocities for nine individual observations at 5000 m depth at Stn. RB. Numerals indicate observation numbers. Also shown is the mean velocity (M) from the long combined record (Fig. 5), with its estimated error at the 95% confidence level (broken line).

though the standard deviation is 1.2 (1.1) times larger than the standard error for the  $u$  ( $v$ ) component, on an average, in the present case.

### 5. Statistics of mesoscale eddies

In some observations, records at both 4000 and 5000 m depths are available at the same station. Their low-pass-filtered daily velocities are very similar to each other and no significant dif-

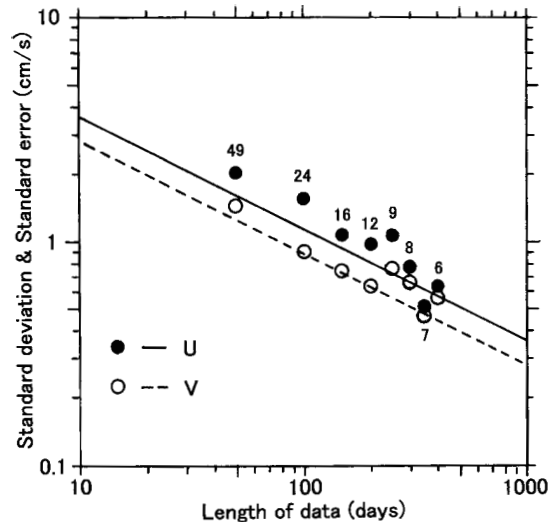


Fig. 8 Dependence of standard deviation of “means” upon the length of data used for their estimations. Each numeral is the number of “means” estimated for a certain data length. Two lines show the standard error  $S_e [= \sigma_0 \sqrt{(\tau_i/T_r)}$  with  $\sigma_0$  and  $\tau_i$  in Table 4] as a function of record length ( $T_r$ ). Dots and the solid line are for  $u$  component, and open circles and the broken line are for  $v$  component. The figure is drawn by utilizing the seven-year long record at Stn. RB.

ferences are recognized in their time series (not shown here); their statistics are basically similar to each other (Table 2). It suggests that the velocity field of mesoscale eddies is almost uniform vertically at abyssal depths.

Figure 9 shows  $K_E$ 's during individual obser-

Table 4. Estimating errors of mean  $u$  and  $v$  components for almost seven years at 5000 m depth at Stn. RB.

	$u$	$v$
Standard deviation $\sigma_0$ (cm s <sup>-1</sup> )	3.1	2.9
Record length $T_r$ (days)	2462	2462
Integral timescale $\tau_i$ (days)	12.3	8.7
Degrees of freedom $N_d$	200	283
Standard error $S_e$ (cm s <sup>-1</sup> )	0.22	0.17
Error on 95% confidence level $\epsilon$ (cm s <sup>-1</sup> )	0.44	0.35
Mean (cm s <sup>-1</sup> )	-0.12 ± 0.44	0.72 ± 0.35

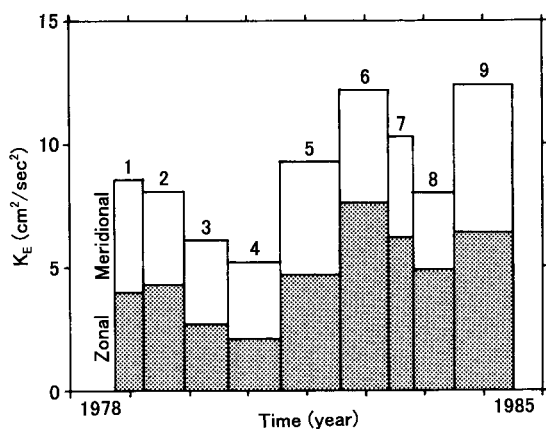


Fig. 9 Eddy kinetic energies during nine individual observations at 5000 m depth at Stn. RB. Numerals indicate observation numbers. Partition of zonal  $K_E$  (shaded box) and meridional  $K_E$  (blank box) is also shown.

vations at Stn. RB (Fig. 5). Fluctuation of the  $K_E$  is large; the maximum  $K_E$  ( $12.4 \text{ cm}^2 \text{ s}^{-2}$ ) is more than two times larger than the minimum  $K_E$  ( $5.2 \text{ cm}^2 \text{ s}^{-2}$ ). The figure also shows the partition of zonal and meridional  $K_E$ 's. Ratios of meridional to zonal  $K_E$ 's vary between 0.6 and 1.4, with a mean of 0.9. The long combined record at Stn. RB (Fig. 5 and Table 3) shows followings. The flow direction of daily velocity changes mostly counterclockwise. The zonal variance ( $10 \text{ cm}^2 \text{ s}^{-2}$ ) is similar to the meridional variance ( $9 \text{ cm}^2 \text{ s}^{-2}$ ). The  $K_E$  ( $9.2 \text{ cm}^2 \text{ s}^{-2}$ ) is more than 30 times larger than the  $K_M$  ( $0.3 \text{ cm}^2 \text{ s}^{-2}$ ). Those statistics are quite similar to the time-space averages of all individual statistics at abyssal depths (Table 2).

For the combined record at Stn. RC (Table 3), the meridional variance ( $19 \text{ cm}^2 \text{ s}^{-2}$ ) is large, which results in large  $K_E$  ( $15 \text{ cm}^2 \text{ s}^{-2}$ ). Those two are also large for individual records (Obs. 1 and 2) compared with other stations (Table 2). For the combined record at Stn. RI, the meridional variance ( $14 \text{ cm}^2 \text{ s}^{-2}$ ) is more than two

times larger than the zonal variance ( $6 \text{ cm}^2 \text{ s}^{-2}$ ). At Stn. RR, both two records (separated by 20 m in vertical) show that the meridional variance ( $22 \text{ cm}^2 \text{ s}^{-2}$ ) is three times larger than the zonal variance ( $7 \text{ cm}^2 \text{ s}^{-2}$ ), which is unique in the present statistics. At Stn. RS, both two records (separated by 20 m in vertical) show large  $K_E$ 's (20 and  $24 \text{ cm}^2 \text{ s}^{-2}$ ), which are about twice of the overall time-space average (Table 2).

## 6. Frequency spectra

The seven-year long velocity record at 5000 m depth at Stn. RB (Fig. 5) gives statistically significant estimates of frequency spectra for the eddy kinetic energy (Fig. 10). Zonal and meridional power spectral densities are estimated from energy densities obtained by the fast Fourier transform method and averaged over 10 frequencies. Hence spectra for the zonal and meridional  $K_E$ 's are regarded as containing 20 degrees of freedom, and their 95 % confidence limits are from 0.58 to 2.1 times individual estimates. The spectrum for the total  $K_E$  is estimated as the sum of those two and therefore, its confidence limits are somewhat narrower than that range.

For convenience, each spectrum is divided into six frequency bands. They are labeled "annual/secular scale," "mesoscale I," "mesoscale II," "mesoscale III," "monthly scale" and "rest." Their period ranges and  $K_E$ 's contained in those bands are shown in Table 5, which also shows ratios of the meridional to zonal  $K_E$ 's.

Most of the total  $K_E$  (78 %) is contained in the mesoscale I, II and III bands (period range of 31-235 days). Therefore, the three bands as a whole could be called an energy-containing or eddy-containing band (MODE GROUP, 1978). In the whole eddy-containing band, the zonal and meridional  $K_E$ 's are equal to each other (both,  $3.5 \text{ cm}^2 \text{ s}^{-2}$ ). In the mesoscale I, the zonal  $K_E$  is

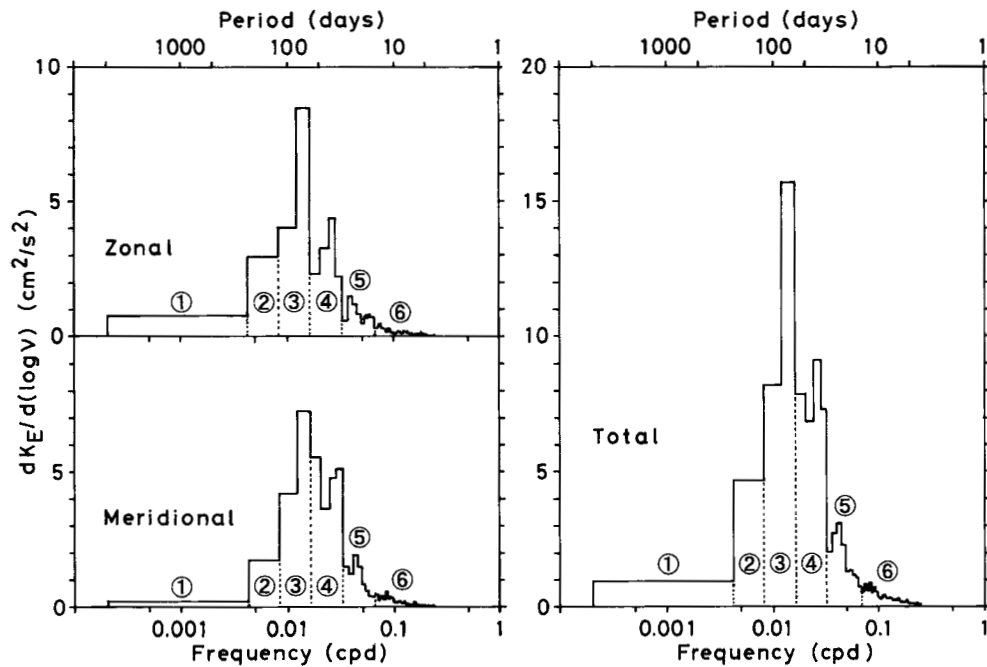


Fig. 10 Frequency spectra of eddy kinetic energy estimated from the seven-year long record at 5000 m depth at Stn. RB (Fig. 5). They are plotted in a variance-preserving form, i.e., an area below the curve represents energy contents in the corresponding frequency range. Symbol  $\nu$  denotes frequency in cycle per day. Spectra of zonal, meridional and total  $K_E$ 's are shown. Each spectrum is divided into six frequency bands, whose ranges are shown by dotted lines and whose reference numbers are indicated by circled numerals. See Table 5 for details.

Table 5. Zonal, meridional and total eddy kinetic energies contained in six frequency bands of the spectra shown in Fig. 10. Also shown are labels of frequency bands, their period ranges, and ratios of meridional to zonal  $K_E$ 's. Small discrepancy among numerals is due to rounding lower digits.

Label of frequency band	Period range (days)	Zonal $K_E$	Meridional $K_E$	Total $K_E$	Ratio
		(cm <sup>2</sup> s <sup>-2</sup> )			
1 Annual/secular scale	235 - 4924	1.0	0.2	1.2	0.2
2 Mesoscale I	120 - 235	0.9	0.5	1.4	0.6
3 Mesoscale II	61 - 120	1.7	1.6	3.4	0.9
4 Mesoscale III	31 - 61	0.9	1.4	2.3	1.6
5 Monthly scale	16 - 31	0.3	0.3	0.6	1.3
6 Rest	2 - 16	0.1	0.1	0.2	1.2
Whole	2 - 4924	4.9	4.2	9.2	0.9

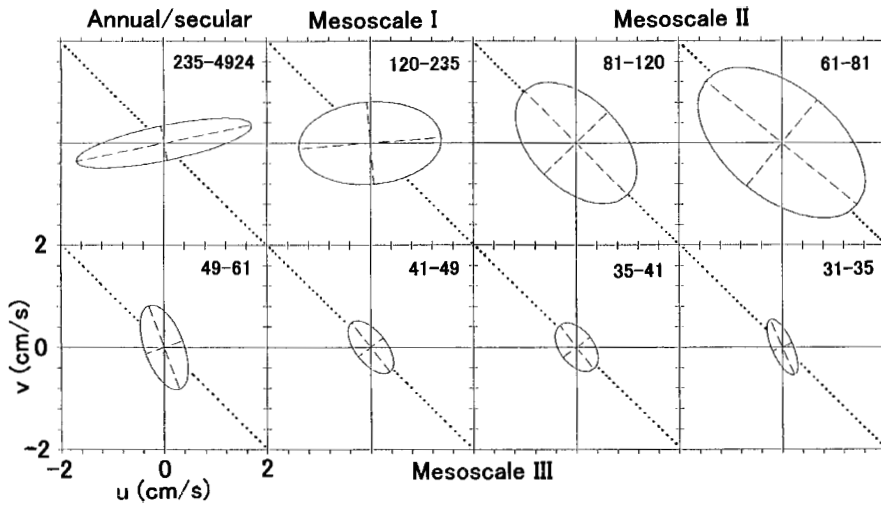


Fig. 11 Current ellipses of lowest eight frequency bands of spectra shown in Fig. 10. Numerals at upper-right corner of each panel show the period range (in days) of that frequency band. Solid lines are  $u$  and  $v$  axes, dashed lines are major and minor axes, and dotted lines indicate the northwest/southeast direction.

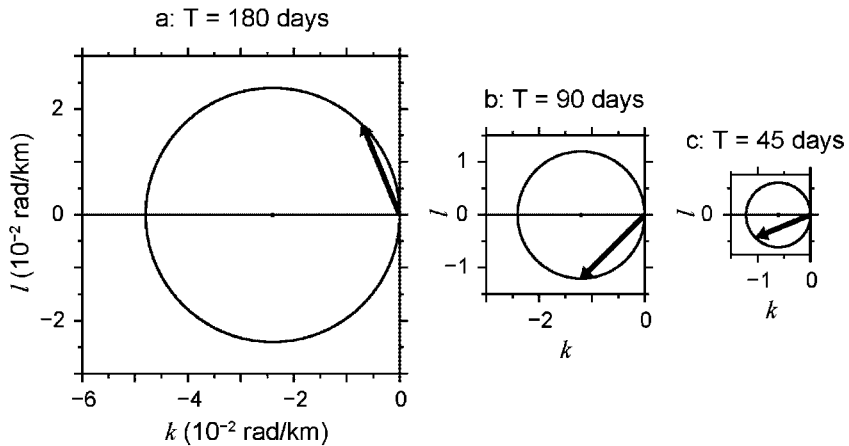


Fig. 12 Conceptual figures of dispersion relation of barotropic Rossby waves (circles) for three periods and selected wavenumber vectors (arrows). Panel (a) is for the period of 180 days and a wavenumber vector directed to the north-northwest with a wavelength of 290 km, (b) for 90 days and the south-west, with 360 km, and (c) for 45 days and the west-southwest, with 570 km. Symbol  $k$  ( $l$ ) denotes the zonal (meridional) wavenumber.

dominant, while in the mesoscale III, the meridional  $K_E$  is dominant. In the mesoscale II, they are almost equal to each other. In the annual/

secular scale, the zonal  $K_E$  is more than four times larger than the meridional  $K_E$ . In the monthly scale, they are almost equal to each oth-

er. In the rest, they are trivially small.

Those spectral features are shown in a different way as current ellipses based on rotary spectrum analysis (Fig. 11). In the annual/secular scale and mesoscale I, the major axis is almost parallel to the  $u$ -axis, and zonal fluctuations are dominant. In the mesoscale II (two panels), the major axis is parallel to the northwest/southeast, and zonal and meridional fluctuations are comparable. In the mesoscale III (four lower panels), the major axis is parallel to the north-northwest/south-southeast, and meridional fluctuations are dominant.

Both zonal dominance in the longer-period bands and meridional dominance in the shorter-period band are understood qualitatively by difference in phase propagation direction of fluctuations, if the fluctuations are assumed as plane barotropic Rossby waves having moderate wavelengths of hundreds of kilometers, as pointed out by IMAWAKI and TAKANO (1982). The assumption of plane waves is supported by MIYAMOTO et al. (2019). Figure 12 shows this situation conceptually. The plane Rossby wave of a longer period (Panel a; mesoscale I) is able to have a wavenumber vector (with a moderate magnitude) directed nearly to the north or south; its associated motion is dominantly zonal. On the other hand, the Rossby wave of a shorter period (Panel c; mesoscale III) is able to have a moderate wavenumber vector directed nearly to the west; its associated motion is dominantly meridional. The Rossby wave of a moderate period (Panel b; mesoscale II) is able to have a moderate wavenumber vector directed to the southwest or northwest; its associated motion is of no dominance. The wavelengths shown in Fig. 12 are similar to those estimated by fitting a set of barotropic Rossby waves to fluctuations at several stations in the present site (IMAWAKI, 1985).

## 7. Vorticity balance

Theoretically, the motion of mid-ocean mesoscale eddies is described as follows. Let  $x$  ( $y$ ) be the eastward (northward) coordinate, and  $(u, v)$  the corresponding velocity components. The Rossby number  $R_o$  is defined as  $U/fL$ , where  $U$  is a characteristic horizontal velocity scale,  $f$  the Coriolis parameter and  $L$  a characteristic horizontal length scale. Taking  $U = 10 \text{ cm s}^{-1}$ ,  $f = 10^{-4} \text{ s}^{-1}$  and  $L = 100 \text{ km}$ , the  $R_o$  is 0.01, which is small enough for equations to be developed in an asymptotic series in  $R_o$ , providing the quasi-geostrophic regime (PEDLOSKY, 1996) as follows.

Under the Boussinesq approximation and hydrostatic approximation, the quasi-geostrophic field is described as follows. The horizontal velocity  $\mathbf{v}$  is expanded as  $\mathbf{v} = \mathbf{v}_0 + \mathbf{v}_1 + \dots$ , where  $\mathbf{v}_0 = (u_0, v_0)$  is the lowest order velocity and  $\mathbf{v}_1$  the first order velocity, being as small as  $R_o \mathbf{v}_0$ . The lowest order velocity  $\mathbf{v}_0$  is in geostrophic balance and horizontally non-divergent.

$$f_0 \mathbf{k}_U \times \mathbf{v}_0 = -\rho^{-1} \nabla p \quad (1)$$

$$\nabla \cdot \mathbf{v}_0 = 0. \quad (2)$$

Here  $\mathbf{k}_U$  is the upward unit-vector perpendicular to the  $x$ - $y$  plane,  $f_0$  the Coriolis parameter at the origin,  $\rho$  the water density and  $p$  the pressure, of the lowest order. The equation for the vertical component of relative vorticity  $\zeta = [v_{0x} - u_{0y}]$  of the lowest order is

$$\zeta_t + \mathbf{v}_0 \cdot \nabla \zeta + \beta v_0 + f_0 \nabla \cdot \mathbf{v}_1 = 0. \quad (3)$$

Here notation  $\phi_t$  means time derivative of a scalar property  $\phi$ , and  $\phi_x$  ( $\phi_y$ ) means  $x$  ( $y$ ) derivative of  $\phi$ . The parameter  $\beta$  is the meridional gradient of Coriolis parameter at the origin;  $\beta$  is  $0.20 \times 10^{-12} \text{ cm}^{-1} \text{ s}^{-1}$  at  $30^\circ \text{ N}$ . Equation (3) shows that the local time change of relative vorticity is

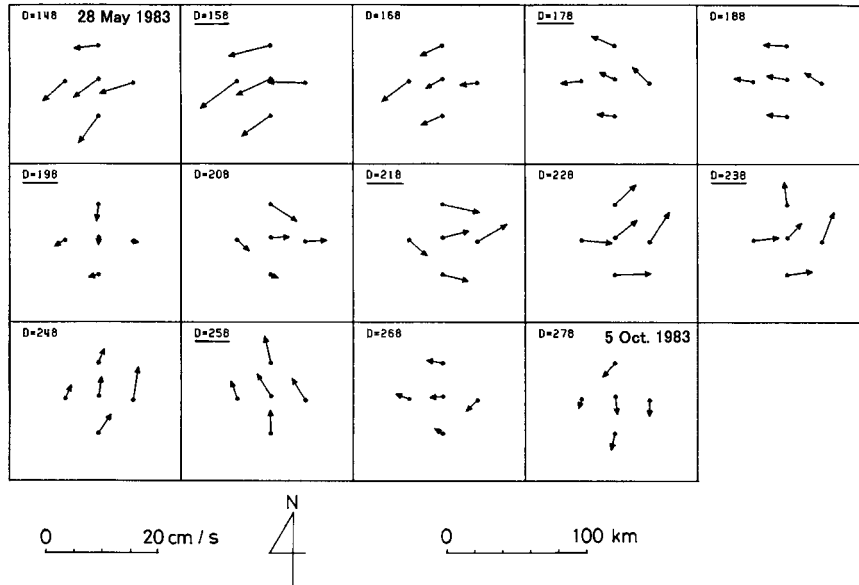


Fig. 13 Sequence of 10-day interval snapshots of 10-day mean velocities at 4000 m depth during Array-83. The year-day of 1983 is shown at the upper-left corner of each panel. On underlined days, vorticity balance is examined.

balanced with the sum of the horizontal advection of relative vorticity, horizontal advection of planetary vorticity (beta-effect) and divergence of the first order horizontal velocity (vertical stretching). If the flow is associated with barotropic planetary Rossby waves, the vorticity equation becomes the linear non-divergent vorticity balance, which is simply

$$\zeta_t + \beta v_0 = 0. \quad (4)$$

On the basis of this theoretical framework, we examine how well the local change of relative vorticity is balanced with the advection of planetary vorticity [Eq. (4)] for actual mesoscale eddies, using the present current-meter data. Observed horizontal velocity  $\mathbf{V}_{obs}$  represents mostly the lowest order velocity  $\mathbf{v}_0$  because the first order velocity  $\mathbf{v}_1$  is too small to be distinguished from measurement error. The diver-

gence of observed horizontal velocity  $\nabla \cdot \mathbf{V}_{obs}$  estimated by finite difference includes an error due to smaller-scale fluctuations which cannot be resolved by the present observations, as well as the measurement error. It means that the calculated divergence may not be zero, although the divergence should be zero theoretically [Eq. (2)]. Therefore, the value of calculated divergence can be regarded as an error in both measurement and finite differencing (IMAWAKI, 1983).

$$\nabla \cdot \mathbf{V}_{obs} = Error. \quad (5)$$

The first three terms in Eq. (3) can be estimated from observed velocities, but the last term (vertical stretching) cannot be estimated directly.

To examine the vorticity balance, field measurements were carried out twice. The first was a set of five stations in a cross pattern centered at

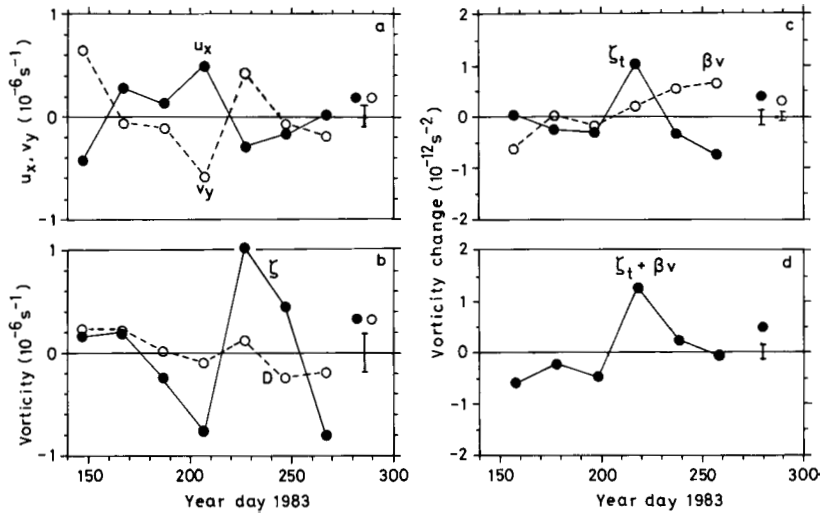


Fig. 14 Time series of various properties concerning the vorticity balance at Stn. RJ during Array-83. Panel (a) is for  $u_{0x}$  (dots) and  $v_{0y}$  (open circles), (b) for  $\zeta$  (dots) and calculated horizontal divergence ( $D$ ; open circles), (c) for  $\zeta_t$  (dots) and  $\beta v_{0y}$  (open circles), and (d) for the sum of these two ( $\zeta_t + \beta v_{0y}$ ). In each panel, vertical bars on the right-hand side indicate corresponding estimated errors.

Stn. RJ with zonal and meridional separations of 24 km (Fig. 1). It was carried out from May through October 1983 as Array-83 (Obs. 7). The second was a set of 13 stations in a diamond shape centered at Stn. RT with separations of 25 km. It was carried out from July 1984 through July 1985 as Array-84 (Obs. 9).

### 7.1 Array-83

Figure 13 shows a sequence of 10-day mean velocities at 4000 m depth during Array-83. Eddies having a speed of  $10 \text{ cm s}^{-1}$  travel in the site. Figure 14 shows variables concerning the vorticity balance at Stn. RJ, at 20-day interval. Estimated variables are temporally independent from each other because the time interval is much longer than integral timescales of  $u$  and  $v$  components (Table 4). In this section, all variables are based on 20-day mean velocities; targeted eddies are having temporal scales of more

than several-tens days (periods longer than the mesoscale III). Horizontal derivatives are estimated by finite difference of velocities with a spatial interval of 48 km, in a straightforward manner. Their error is estimated to be  $0.09 \times 10^{-6} \text{ s}^{-1}$  from the error ( $0.3 \text{ cm s}^{-1}$ ) of  $u$  and  $v$  components. The station-spacing is fine enough compared with the typical horizontal scale of fluctuations, which is inferred from the lag (70–90 km) of first zero-crossing of transverse correlation function of velocity fluctuations.

After subtracting averages during the array observation, horizontal derivatives  $u_{0x}$  and  $v_{0y}$  are estimated [Fig. 14 (a)]. They have generally opposite signs and almost equal magnitudes; their correlation coefficient ( $-0.89$ ) is very high in magnitude, and standard deviations of  $u_{0x}$  and  $v_{0y}$  are almost the same, suggesting that they are balanced well with each other. Horizontal divergence calculated from the two is shown in

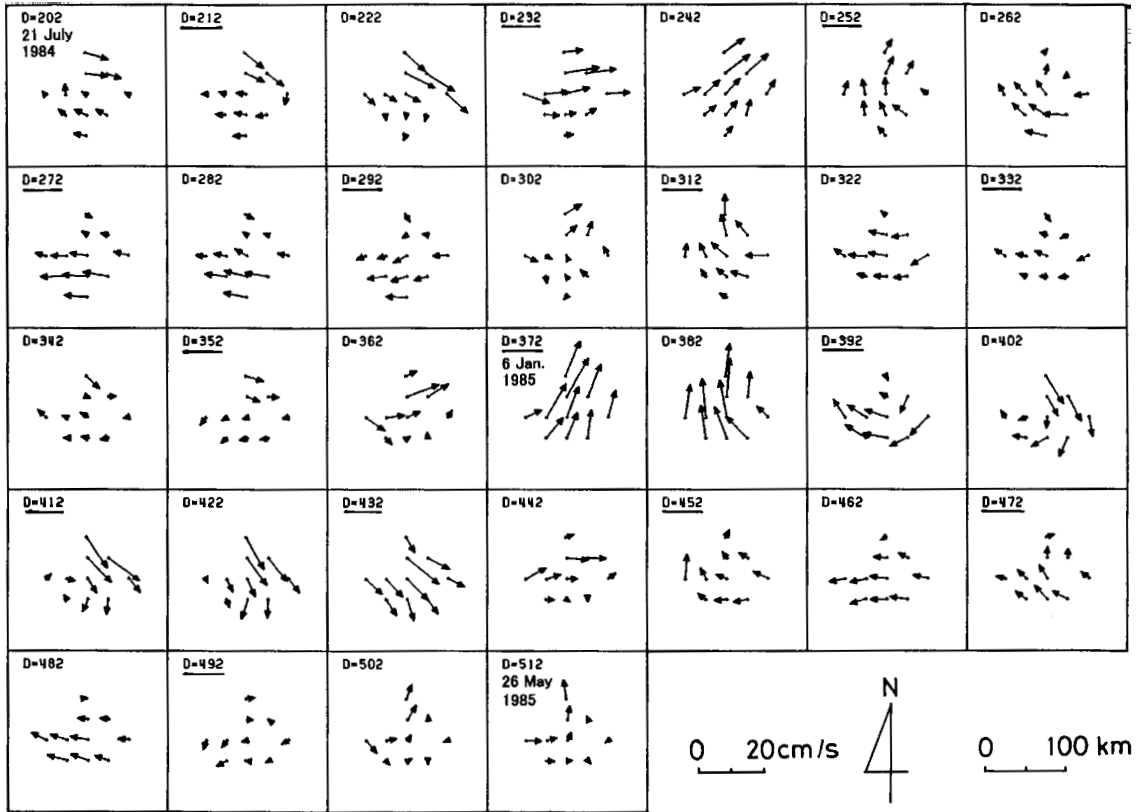


Fig. 15 Same as Fig. 13, but for Array-84 and serial year-day of 1984. At Stns. RB and RR, velocities at 5000 and 4100 m depths, respectively are used.

Fig. 14 (b). As shown in Eq. (5), the calculated divergence is regarded as an error; i.e., its standard deviation ( $0.18 \times 10^{-6} \text{ s}^{-1}$ ) gives the error in addition or subtraction of two similar horizontal derivatives. Figure 14 (b) also shows the estimated relative vorticity  $\zeta$ . Its standard deviation ( $0.61 \times 10^{-6} \text{ s}^{-1}$ ) is more than three times larger than the estimated error.

The local change of relative vorticity  $\zeta_t$  is estimated from difference of  $\zeta$ 's separated by 20 days. The advection of planetary vorticity  $\beta v_0$  is estimated from the  $v$  component at Stn. RJ. Those two are shown in Fig. 14 (c). The standard deviation of  $\beta v_0$  ( $0.43 \times 10^{-12} \text{ s}^{-2}$ ) is not much different from that of  $\zeta_t$  ( $0.54 \times 10^{-12} \text{ s}^{-2}$ ),

but their correlation coefficient ( $-0.27$ ) is rather low. Figure 14 (d) shows the sum of these two, which is the departure from the linear non-divergent vorticity balance [Eq. (4)]. The sum is small in half of six cases (for year-days 178, 238 and 258), being below or close to its estimated error ( $0.15 \times 10^{-12} \text{ s}^{-2}$ ), but large in other cases, especially on year-day 218, for which a large increase of  $\zeta$  from year-days 208 to 228 cannot be accounted for by  $\beta v_0$ . The horizontal advection of relative vorticity cannot be estimated from the Array-83 data.

As conclusion of this subsection, the local change of relative vorticity is balanced basically with the advection of planetary vorticity but oc-

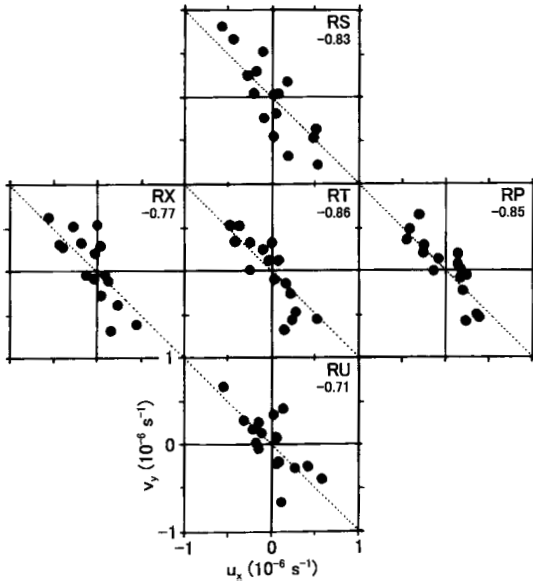


Fig. 16 Scatter plots of  $u_{0x}$  versus  $v_{0y}$  at five stations, whose names are shown at the upper-right corner of each panel, during Array-84. Numerals below station names are correlation coefficients of 16 cases each. Dotted lines indicate the perfect out-of-phase correlation.

asionally some unknown terms are required to complete the vorticity balance.

## 7.2 Array-84

Figure 15 shows a sequence of 10-day mean velocities at 4000 m depth during Array-84. The flow is very smooth horizontally and organized well; for example, velocity vectors are like a school of swimming-fish on year-days 242, 372 and 432, and well-organized anticyclonic eddies are seen on year-days 252 and 402. The flow is dominated by anticyclonic patterns. It is because the flow is heavily biased by the steady vortex (Fig. 6) having strong negative vorticity of  $-1.1 \times 10^{-6} \text{ s}^{-1}$  at Stn. RT and RP (IMAWAKI and TAKANO, 2019). Time series of daily velocities at all stations show that the flow direction changes mostly counterclockwise (not shown here).

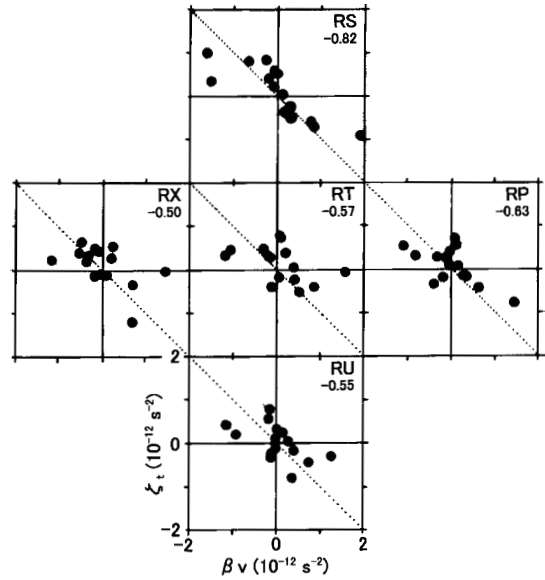


Fig. 17 Same as Fig. 16, but for plots of  $\beta v_0$  versus  $\zeta_t$ , and 15 cases.

In the following analysis, missing data at Stn. RP (RW) are filled by averaging data from Stns. RO, RN, RQ and RT (RR and RB). At Stn. RV, data are available only during first 135 days, and so we are forced to use data extrapolated linearly from Stns. RT and RU for the remaining period. At Stns. RX and RY, the usable data stopped before the end of array observation, and so the analysis on vorticity balance is stopped at that time (year-day 525).

After subtracting averages during the array observation, analysis similar to Array-83 is carried out for Stns. RS, RP, RT, RX and RU, using data at five nearby stations separated by 25 km. The results are shown as scatter plots (Figs. 16 and 17). Horizontal derivatives  $u_{0x}$  and  $v_{0y}$  have generally opposite signs and almost equal magnitudes (Fig. 16). Their correlation coefficients are very high in magnitude at all five stations. For the overall average of 80 cases, the correlation coefficient is  $-0.80$ , and standard deviations of  $u_{0x}$  and  $v_{0y}$  are similar to each other, suggesting

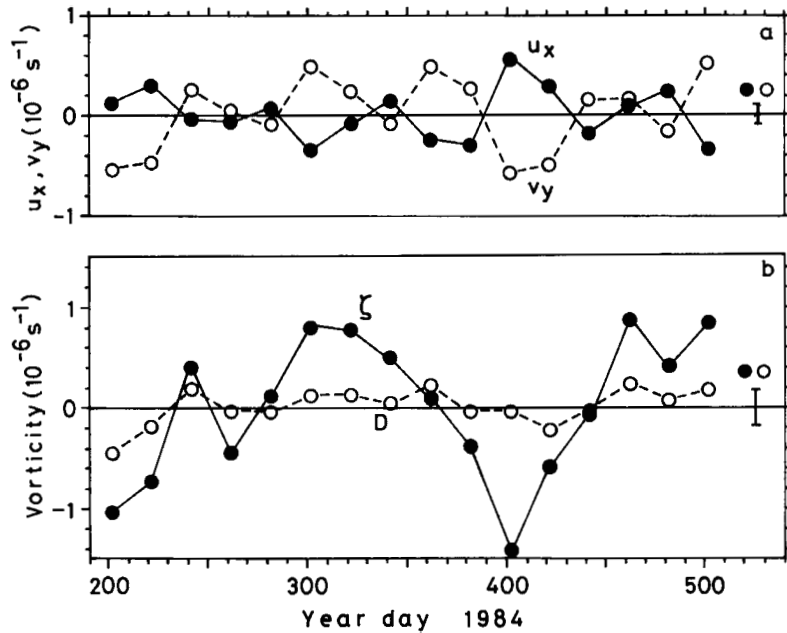


Fig. 18 Time series of properties concerning the vorticity balance at Stn. RT during Array-84. Panel (a) is for  $u_{0x}$  (dots) and  $v_{0y}$  (open circles), and (b) for  $\zeta$  (dots) and calculated horizontal divergence ( $D$ ; open circles). In each panel, a vertical bar on the right-hand side indicates corresponding estimated error.

that the two variables are balanced very well.

Vorticity balances between the local change of relative vorticity  $\zeta_t$  and advection of planetary vorticity  $\beta v_0$  at the five stations are shown in Fig. 17. The two properties have generally opposite signs and almost equal magnitudes. Their correlation coefficients are high at Stn. RS. They are not so high at other stations but significantly different from zero at the 95 % confidence level. The overall correlation coefficient of 75 cases is  $-0.61$ , which is high enough in magnitude to be significantly different from zero at the 95 % confidence level. The overall standard deviation of  $\zeta_t$  is  $0.65 \times 10^{-12} \text{ s}^{-2}$  and that of  $\beta v_0$  is  $0.45 \times 10^{-12} \text{ s}^{-2}$ .

The same results as the scatter plot for Stn. RT in Fig. 16 are shown as time series of  $u_{0x}$  and  $v_{0y}$  in Fig. 18 (a). They have generally opposite

signs and similar magnitudes; their correlation coefficient ( $-0.86$ ) is very high in magnitude and standard deviations of  $u_{0x}$  and  $v_{0y}$  are similar to each other, suggesting well-balanced variations. The time series of sum of the two, namely the calculated horizontal divergence is shown in Fig. 18 (b); its standard deviation ( $0.18 \times 10^{-6} \text{ s}^{-1}$ ) gives the error of the relative vorticity  $\zeta$  and is numerically the same as the corresponding one in Array-83. The standard deviation of  $\zeta$  ( $0.69 \times 10^{-6} \text{ s}^{-1}$ ) is almost four times larger than the error.

Similarly, the same results as the scatter plot for Stn. RT in Fig. 17 are shown as time series of  $\zeta_t$  and  $\beta v_0$  in Fig. 19 (a). Their correlation coefficient ( $-0.57$ ) is significantly different from zero at the 95 % confidence level as mentioned above. The standard deviation of  $\beta v_0$  ( $0.64 \times 10^{-12} \text{ s}^{-2}$ )

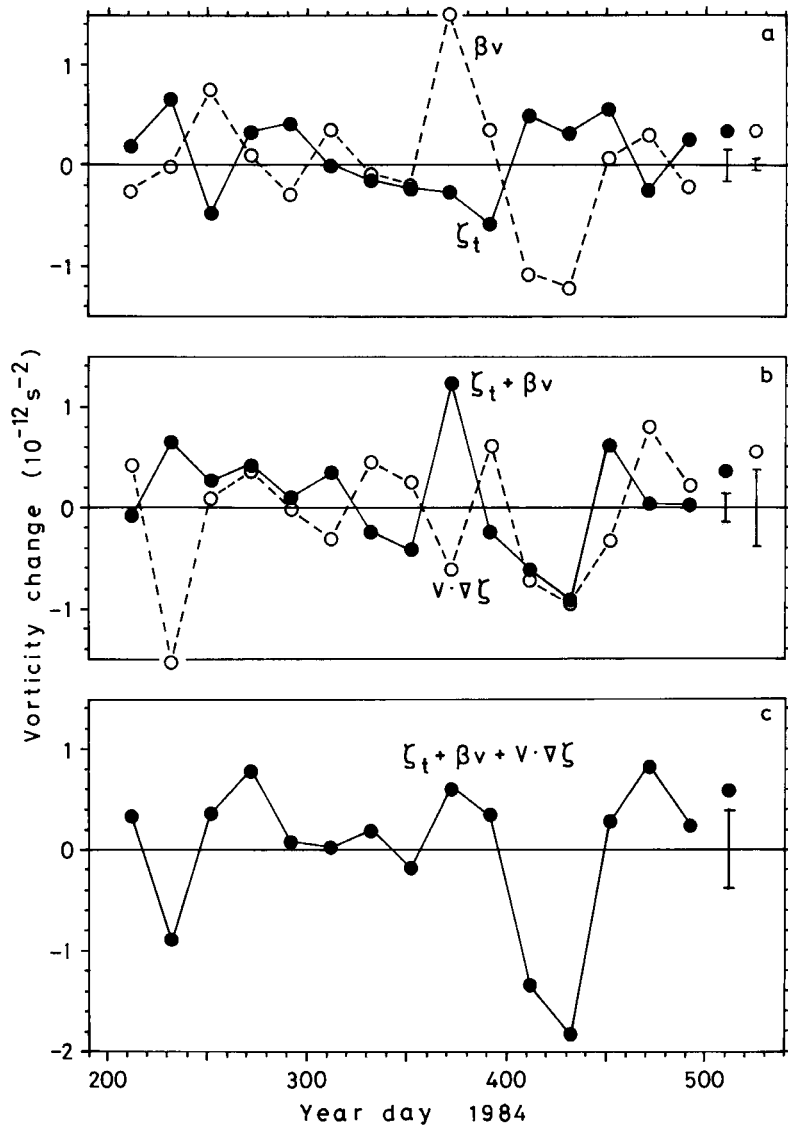


Fig. 19 Time series of various terms of vorticity balance at Stn. RT during Array-84. Panel (a) is for  $\zeta_t$  (dots) and  $\beta v_0$  (open circles), (b) for the sum of these two ( $\zeta_t + \beta v_0$ ; dots) and advection of relative vorticity ( $\mathbf{v}_0 \cdot \nabla \zeta$ ; open circles), and (c) for the sum of those three ( $\zeta_t + \beta v_0 + \mathbf{v}_0 \cdot \nabla \zeta$ ). In each panel, vertical bars on the right-hand side indicate corresponding estimated errors.

is larger than that of  $\zeta_t$  ( $0.38 \times 10^{-12} \text{ s}^{-2}$ ). The sum of these two [Fig. 19 (b)] is small in about half of 15 cases (for year-days 212, 252, 292, 332, 392, 472 and 492), being below or close to its esti-

estimated error ( $0.15 \times 10^{-12} \text{ s}^{-2}$ ), but large on year-days 232, 372, 412, 432 and 452. Especially on year-days 372, 412 and 432, the  $\zeta_t$  is overbalanced by the large  $\beta v_0$ .

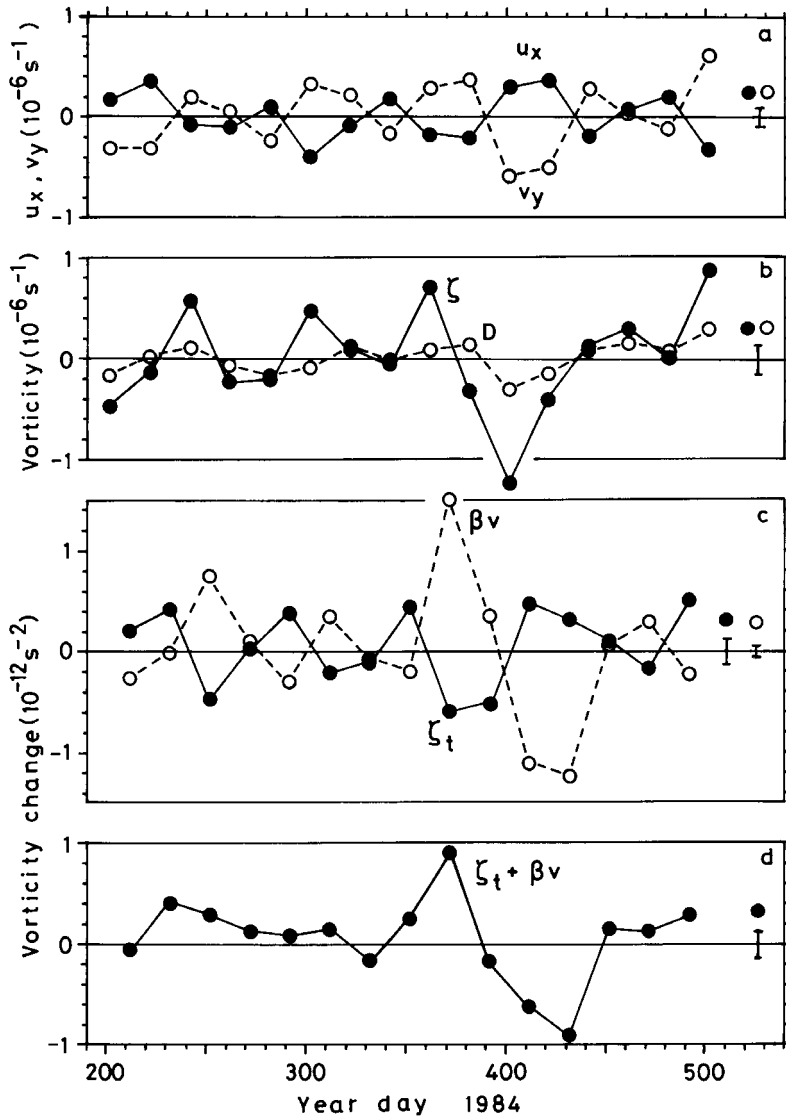


Fig. 20 Same as Fig. 14, but for Stn. RT during Array-84, using data at Stns. RR, RN, RV, RB and RT to examine a larger-scale balance.

Figure 19 (b) also shows the horizontal advection of relative vorticity  $\mathbf{v}_0 \cdot \nabla \zeta$ , estimated from the velocity at Stn. RT and gradient of  $\zeta$  over Stns. RS, RP, RU and RX. The advection of  $\zeta$  accounts for the above sum ( $\zeta_t + \beta v_\theta$ ) to some extent in several cases (for year-days 312, 332, 352, 372, 392 and 452), but does not account for

in other cases, having large negatives (for year-days 232, 412 and 432). In short, the horizontal advection of relative vorticity accounts for the imbalance between the local change of relative vorticity and advection of planetary vorticity in some cases, but makes the imbalance worse in other cases.

Finally, the vorticity balance is examined on a larger scale, using data at five stations separated by 50 km, namely Stns. RR, RN, RV, RB and RT. Time series of  $u_{0x}$  and  $v_{0y}$  at Stn. RT are shown in Fig. 20 (a). They have generally opposite signs and almost equal magnitudes; their correlation coefficient ( $-0.92$ ) is very high in magnitude and standard deviations of  $u_{0x}$  and  $v_{0y}$  are almost the same. Figure 20 (b) shows the horizontal divergence calculated from the two and  $\zeta$ ; the standard deviation of  $\zeta$  ( $0.50 \times 10^{-6} \text{ s}^{-1}$ ) is much larger than that of horizontal divergence ( $0.15 \times 10^{-6} \text{ s}^{-1}$ ), which gives the error of  $\zeta$ . The  $\beta v_0$  (the same as the smaller scale) and  $\zeta_t$  are shown in Fig. 20 (c). Their correlation coefficient ( $-0.80$ ) is much higher in magnitude than the smaller scale. The standard deviation of  $\beta v_0$  is larger than that of  $\zeta_t$  ( $0.37 \times 10^{-12} \text{ s}^{-2}$ ). The sum of these two [Fig. 20 (d)] is small in about half of 15 cases but large on year-days 372, 412 and 432, where  $\zeta_t$  is again over-balanced by the large  $\beta v_0$ . The relation between the two is a little better on the larger scale than smaller scale.

As conclusion of this subsection, the local change of relative vorticity is balanced basically with the advection of planetary vorticity on both smaller and larger scales. In some cases, the horizontal advection of relative vorticity accounts for the imbalance between the two, but makes it worse in other cases; the vorticity balance of mesoscale eddies has not yet been completed.

## 8. Discussions

Records at 5000 m depth at Stn. RI show a stable north-northwestward flow. The station is located at 40 km east of Stn. TA ( $30^\circ 00'N$ ,  $145^\circ 45'E$ ), where a strong south-southeastward mean flow along local isobaths was observed during 1978–1982, with bottomward intensification, namely the speed increase from  $3.2 \text{ cm s}^{-1}$  at

4000 m depth to  $7.2 \text{ cm s}^{-1}$  at 5800 m depth (50 m above the bottom) (Keisuke Taira, personal communication; Miyamoto et al., 2019). The stable flow at Stn. RI might be a part of the local circulation associated with this strong flow at Stn. TA.

Records at 4100 m depth level at Stn. RR show unique dominance of the meridional variance over zonal variance. As shown in Fig. 1, the station is located at the foot of western slope of the seamount, which rises from 6300 m deep bottom up to 5400 m depth. The meridional dominance is probably due to preference of fluctuating flows along local isobaths, although a remarkable mean flow associated with the steady vortex is directed to the seamount (Fig. 6). This local dominance of meridional variance could disturb the examination of vorticity balance but the possible distortion is not apparent in the Array-84 analysis.

A long velocity record for almost seven years was obtained at 5000 m depth at Stn. RB. This is probably one of the longest continuous records from moored current-meters at depth in the mid-ocean over the world, together with a similar long record at 1000 m depth in the eastern North Atlantic, where moorings were maintained during 1980–1986 (ZENK and MÜLLER, 1988). The mean  $v$  component ( $0.72 \text{ cm s}^{-1}$ ) at 5000 m depth at Stn. RB is almost exactly equal to that of time-space average ( $0.71 \text{ cm s}^{-1}$ ) of statistics of all records at abyssal depths in the present site, the mean  $u$  component of the former ( $-0.12 \text{ cm s}^{-1}$ ) is close to that of the latter ( $-0.29 \text{ cm s}^{-1}$ ), and the  $K_E$  of the former ( $9.2 \text{ cm}^2 \text{ s}^{-2}$ ) is similar to that of the latter ( $10.8 \text{ cm}^2 \text{ s}^{-2}$ ), suggesting that the record at Stn. RB represents the flow field at the present site quite well. On the other hand, the mean velocity at Stn. RB might be under the effect of the local steady vortex (Fig. 6; IMAWAKI and TAKANO, 2019). Therefore, it

is hard to definitely judge its representativeness of the site.

The eddy kinetic energy is compared with other locations. The level of  $K_E$  at the present site ( $11 \text{ cm}^2 \text{ s}^{-2}$ ) is comparable with that ( $12 \text{ cm}^2 \text{ s}^{-2}$ ) at 4000 m depth at similar latitudes along  $152^\circ \text{ E}$  (SCHMITZ, 1984). The present level is higher than that in the central North Pacific (TAFT *et al.*, 1981) but lower than that in the Kuroshio Extension (SCHMITZ, 1984). It is comparable with the level of  $K_E$  at abyssal depths in the MODE area (Schmitz, 1978). At Stn. RC, the  $K_E$  is large, which might be due to the fact that the station is relatively near to the Kuroshio Extension, considering that the  $K_E$  at 4000 m depth along  $152^\circ \text{ E}$  has the maximum ( $45 \text{ cm}^2 \text{ s}^{-2}$ ) at  $35^\circ \text{ N}$ , namely the vicinity of the upper layer expression of the Kuroshio Extension (SCHMITZ, 1984).

The spectral features of mesoscale eddies obtained in this study are compared with those of the three-year long first-half of the present record (IMAWAKI and TAKANO, 1982). All the major features of the first-half spectra are found in the present spectra, with a finer resolution and in a wider frequency range. The spectral analysis shows zonal dominance of eddy motions in longer-period bands and meridional dominance in the shorter-period band. If the fluctuations are associated with barotropic Rossby waves, the dominance is understood in the vorticity balance [Eq. (4)] as follows. If the period of waves is longer (shorter), the local change of relative vorticity  $\zeta_t$  is smaller (larger) and therefore, the advection of planetary vorticity  $\beta v_\theta$  is smaller (larger), which means the meridional component  $v_\theta$  is smaller (larger), i.e., the zonal (meridional) fluctuations are dominant. Those spectral features are also seen in spectra at 4000 m depth in the western North Atlantic (RICHMAN *et al.*, 1977), although zonal dominance of energy

in the annual scale is not definite. The zonal dominance of eddy fields in longer periods has been suggested by theoretical works (e.g., RHINES, 1977). On the other hand, the meridional eddy kinetic energy is dominant in the temporal mesoscale band and even in the annual band at 1000 m depth in the eastern North Atlantic (ZENK and MÜLLER, 1988).

Concerning the vorticity balance, the local change of relative vorticity is balanced primarily with the advection of planetary vorticity, although the advection of relative vorticity and higher-order divergence may play some role in the balance. It is consistent with the earlier results (IMAWAKI, 1983) obtained by using 10-day mean velocities at 5000 m depth at five stations in the present site, whose station-spacing is somewhat similar to the present larger scale examination.

The present study shows that mesoscale eddies at abyssal depths in mid-ocean are understood basically as fluctuations associated with plane barotropic Rossby waves. Recent studies show that mesoscale fluctuations at the present site having specific spectral peaks are explained by topographic Rossby waves better than planetary Rossby waves (MIYAMOTO *et al.*, 2017; 2019); the former are influenced by the topographic beta-effect as well as planetary beta-effect. In the present analyses, topographic Rossby waves are indistinguishable from barotropic planetary Rossby waves. It is because wavelengths cannot be estimated from single-station data and therefore, the dispersion relation of Rossby waves cannot be used for comparison. It is also because the higher-order divergence in the vorticity balance, where the effect of bottom topography appears as well as the baroclinicity, does not seem to be estimated reliably as the residual of first three terms of Eq. (3).

In examination of vorticity balance during

Array-84, missing data at three stations are made up for by linearly interpolated or extrapolated data. Scatter plots of  $u_{0x}$  versus  $v_{0y}$  and  $\beta v_0$  versus  $\zeta_t$  at five stations using those data (Figs. 16 and 17) do not show any difference among stations. Therefore, the interpolation and extrapolation seem to have worked well. Objective analysis may improve filling the missing data as well as spatial smoothing.

## 9. Summary

Velocities at abyssal depths were measured by moored current-meters in mid-ocean of the western North Pacific during 1978–1985. Current-meters were moored mostly at 4000 and 5000 m depths at various locations for several months to one year repeatedly, providing 50 velocity records. In the raw data, inertial oscillations are apparent as well as diurnal and semi-diurnal tidal fluctuations. Those high-frequency fluctuations are filtered out numerically and low-pass-filtered daily velocities are used for the present analyses.

Time-space averages of statistics of 47 individual records at abyssal depths show followings. The average zonal and meridional velocity-components are less than  $1 \text{ cm s}^{-1}$  in magnitude. The average zonal and meridional variances are almost equal to each other. The eddy kinetic energy is about 40 times larger than the mean kinetic energy. Those statistics confirm that the site is located in typical mid-ocean apart from intense current zones. Both mean velocities and fluctuating velocities at abyssal depths at the same station are similar to each other.

A long velocity record for almost seven years was obtained at 5000 m depth at Stn. RB. This is probably one of the longest continuous records from moored current-meters at depth in the mid-ocean over the world. The overall mean velocity is directed to the north with a speed of less than

$1 \text{ cm s}^{-1}$ . The mean meridional velocity-component is positive significantly at the 95 % confidence level, while the mean zonal component is not significantly different from zero. The zonal variance is similar to the meridional variance. The eddy kinetic energy is more than 30 times larger than the mean kinetic energy. Those statistics are quite similar to the time-space averages of all individual statistics at abyssal depths mentioned above, suggesting that the long record at Stn. RB represents the flow field at the present site quite well, although the mean velocity might be under the effect of the local steady vortex.

This long velocity record at Stn. RB gives statistically significant estimates of frequency spectra for the eddy kinetic energy. Most of the eddy kinetic energy is contained in mesoscale bands I, II and III (period-range of 31–235 days). In the three bands as a whole, zonal and meridional energies are almost equal to each other. In the mesoscale I (120–235 days) the zonal energy is dominant, while in the mesoscale III (31–61 days) the meridional energy is dominant. In the annual/secular scale (295–4924 days) the zonal energy is highly dominant. Both zonal dominance in longer-period bands and meridional dominance in the shorter-period band are understood qualitatively by difference in phase propagation direction of fluctuations, if the fluctuations are assumed as plane barotropic Rossby waves having wavelengths of hundreds of kilometers.

The vorticity balance of mesoscale eddies is examined by using those current-meter data. Relative vorticity is estimated from horizontal derivatives of 20-day mean velocities. Its local change during 20 days is compared with the advection of planetary vorticity, at five stations, providing 75 independent comparison cases. The overall correlation coefficient between the two properties of those cases is  $-0.61$ , which is high

enough to be significantly different from zero at the 95 % confidence level. The overall standard deviations of the two are not much different from each other. Therefore, the local change of relative vorticity is balanced primarily with the advection of planetary vorticity, although the advection of relative vorticity and higher-order horizontal divergence may play some role in the balance.

Those results suggest that mid-ocean mesoscale eddies at abyssal depths are understood as primarily plane barotropic Rossby waves with possible modification.

### Acknowledgements

We thank Mr. Masatoshi Miyamoto of the University of Tokyo for informing the ETOPO1 bottom topography. We are grateful to two anonymous reviewers and Prof. Masahisa Kubota of Tokai University for careful and critical reading of the manuscript and valuable comments. We also thank Mr. Keith Bradley of the Woods Hole Oceanographic Institution (at that time) for introducing SI to the mooring technique. [Affiliation is hereafter understood “at that time.”] The mooring observations were carried out under the lead of KT of the Institute of Physical and Chemical Research and later of the University of Tsukuba with collaboration of SI of Kyoto University. We thank Mr. Satoshi Murata of the University of Tsukuba for his helpful assistance. Mooring deployment and recovery were carried out on board the research vessel *Hakuho Maru* of the University of Tokyo, the research and training vessels *Tokaidaiigaku Maru II* and *Bosei Maru II* of Tokai University (Table 1). We thank Captains and crews of those vessels for their earnest cooperation. The current measurements were done as a pre-operational survey for the disposal of low-level radioactive wastes, financially supported by the Science and Technology

Agency through the Radioactive Waste Management Center. The data were processed at the Data Processing Center of Kyoto University. The work was partly supported by Grants-in-Aid from the Ministry of Education, Science and Culture. The present low-pass-filtered velocities are available at the Website of Japan Oceanographic Data Center; <http://www.jodc.go.jp/jodcweb/JDOSS/>.

### References

- AMANTE, C. and B. W. EAKINS (2009): ETOPO1 1 Arc-Minute Global Relief Model: Procedures, Data Sources and Analysis. NOAA Technical Memorandum NESDIS NGDC-24. National Geophysical Data Center, NOAA. doi: 10.7289/V5C8276M.
- CREASE, J. (1962): Velocity measurements in the deep water of the western North Atlantic, summary. *J. Geophys. Res.*, **67**, 3173–3176.
- FU, L.-L. and R. MORROW (2013): Remote sensing of the global ocean circulation. *In* Ocean Circulation and Climate: A 21st Century Perspective. G. SIEDLER, S. M. GRIFFIES, J. GOULD and J. A. CHURCH (eds.), Academic Press, London, pp. 83–111.
- GODIN, G. (1972): *The Analysis of Tides*. Liverpool University Press, 264 pp.
- GREENE, A. D., D. R. WATTS, G. G. SUTYRIN and H. SASAKI (2012): Evidence of vertical coupling between the Kuroshio Extension and topographically controlled deep eddies. *J. Mar. Res.*, **70**, 719–747, doi: 10.1357/002224012806290723.
- HEINMILER, R. H. (1976): *Mooring Operations Techniques of the Buoy Project at the Woods Hole Oceanographic Institution*, W.H.O.I. Technical Report 76-69. Woods Hole Oceanographic Institution, Woods Hole, Massachusetts, 94 pp.
- IMAWAKI, S. (1983): Vorticity balance for mid-ocean mesoscale eddies at an abyssal depth. *Nature*, **303**, 606–607, doi: 10.1038/303606a0.
- IMAWAKI, S. (1985): Features of mesoscale eddies in the deep mid-ocean of the western North Pacific. *Deep-Sea Res.*, **32**, 599–611, doi: 10.1016/0198-0149(85)90046-9.
- IMAWAKI, S. and K. TAKANO (1982): Low-frequency

- eddy kinetic energy spectrum in the deep western North Pacific. *Science*, **216**, 1407–1408, doi: 10.1126/science.216.4553.1407.
- IMAWAKI, S. and K. TAKANO (2019): Steady vortex observed by moored current-meters at 4000 m depth in the western North Pacific. (to be published)
- KAWABE, M. and S. FUJIO (2010): Pacific Ocean circulation based on observation. *J. Oceanogr.*, **66**, 389–403, doi: 10.1007/s10872-010-0034-8.
- KEFFER, T. (1983): Time-dependent temperature and vorticity balances in the Atlantic North Equatorial Current. *J. Phys. Oceanogr.*, **13**, 224–239.
- MCWILLIAMS, J. C. (1976): Maps from the Mid-Ocean Dynamics Experiment: Part II. Potential vorticity and its conservation. *J. Phys. Oceanogr.*, **6**, 828–846.
- MCWILLIAMS, J. C. and G. R. FLIERL (1976): Optimal, quasi-geostrophic wave analyses of MODE array data. *Deep-Sea Res.*, **23**, 285–300.
- MIYAMOTO, M., E. OKA, D. YANAGIMOTO, S. FUJIO, G. MIZUTA, S. IMAWAKI, M. KUROI and H. HASUMI (2017): Characteristics and mechanism of deep mesoscale variability south of the Kuroshio Extension. *Deep-Sea Res. I*, **123**, 110–117, doi: 10.1016/j.dsr.2017.04.003.
- MIYAMOTO, M., E. OKA, D. YANAGIMOTO, S. FUJIO, M. NAGASAWA, G. MIZUTA, S. IMAWAKI, M. KUROI and H. HASUMI (2019): Topographic Rossby waves at two different periods in the Northwest Pacific Basin. (to be published)
- MODE GROUP (1978): The Mid-Ocean Dynamics Experiment. *Deep-Sea Res.*, **25**, 859–910.
- NILER, P. (2001): The world ocean surface circulation. *In* *Ocean Circulation and Climate: Observing and Modelling the Global Ocean*. G. Siedler, J. Church, and J. Gould (eds.), Academic Press, London, pp. 193–204.
- PEDLOSKY, J. (1996): *Ocean Circulation Theory*. Springer-Verlag, Berlin, 453 pp.
- PRICE, J. F. and H. T. ROSSBY (1982): Observations of a barotropic planetary wave in the western North Atlantic. *J. Mar. Res.* **40**, suppl., 543–558.
- RHINES, P. B. (1977): The dynamics of unsteady currents. *In* *The Sea: Ideas and Observations on Progress in the Study of the Seas*, Vol. 6. E. D. GOLDBERG, I. N. MCCAIVE, J. J. O'BRIEN and J. H. STEEL (eds.), Wiley, New York, pp. 189–318.
- RICHMAN, J. G., C. WUNSCH and N. G. HOGG (1977): Space and time scales of mesoscale motion in the western North Atlantic. *Rev. Geophys. and Space Phys.*, **15**, 385–420.
- ROBINSON, A. R. (ed.) (1983): *Eddies in Marine Science*. Springer-Verlag, Berlin, 609 pp.
- SCHMITZ, W. J., Jr. (1978): Observations of the vertical distribution of low frequency kinetic energy in the western North Atlantic. *J. Mar. Res.*, **36**, 295–310.
- SCHMITZ, W. J., Jr. (1984): Abyssal eddy kinetic energy levels in the western North Pacific. *J. Phys. Oceanogr.*, **14**, 198–201.
- TAFT, B. A., S. R. RAMP, J. G. DWORSKI and G. HOLLOWAY (1981): Measurements of deep currents in the central North Pacific. *J. Geophys. Res.*, **86**, 1955–1968.
- TALLEY, L. D., G. L. PICKARD, W. J. EMERY and J. H. SWIFT (2011): *Descriptive Physical Oceanography: An Introduction*, Sixth Edition. Elsevier, London, 555 pp.
- UCHIDA, H. and S. IMAWAKI (2003): Eulerian mean surface velocity field derived by combining drifter and satellite altimeter data. *Geophys. Res. Lett.*, **30**, 1229, doi: 10.1029/2002GL016445.
- ZENK, W. and T. J. MÜLLER (1988): Seven-year current meter record in the eastern North Atlantic. *Deep-Sea Res. A*, **35**, 1259–1268, doi.org/10.1016/0198-0149(88)90082-9.

*Received: September 19, 2018*

*Accepted: December 20, 2018*